Ore Geology Reviews xxx (xxxx) 104633

Contents lists available at ScienceDirect

Ore Geology Reviews

journal homepage: www.elsevier.com/locate/oregeorev

# The Shepherd Mountain iron ore deposit in Southeast Missouri, USA – An extension of the Pilot Knob magmatic-hydrothermal ore system: Evidence from iron oxide chemistry

Bolorchimeg N. Tunnell [a], Marek Locmelis [b,*], Cheryl Seeger [c], Marilena Moroni [d], Sarah Dare [e], Ryan Mathur [f], Brandon Sullivan [b]

[a] Department of Geology and Hydrogeology, School of Geology and Mining Engineering, Mongolian University of Science & Technology, Ulaanbaatar, Mongolia
[b] Department of Geosciences and Geological and Petroleum Engineering, Missouri University of Science & Technology, Rolla, MO 65409, USA
[c] Missouri Department of Natural Resources, Missouri Geological Survey, USA
[d] Department of Earth Sciences, University of Milan, Italy
[e] Département de Sciences Appliquées, Université du Québec á Chicoutimi, QC G7H 2B1, Canada
[f] Juniata College, 1700 Moore St, Huntingdon, PA 16652, USA

ARTICLE INFO

*Keywords:*
Iron isotopes
LA-ICP-MS
Silician magnetite
Mushketovite
Oscillatory zoning
Critical Minerals

ABSTRACT

The Southeast Missouri Iron Metallogenic Province in the Midcontinent USA contains seven major and several minor IOA/IOCG-type deposits and a series of shallow vein-type deposits/prospects, all of which are spatially and temporally associated with early Mesoproterozoic (1500–1440 Ma) magmatism in the St. Francois Mountains terrane. One of the vein-type deposits is the Shepherd Mountain deposit, which consists of two northeast-trending ore veins dominated by magnetite and lesser amounts of hematite. Here we report the findings of a study that investigates the origin of the Shepherd Mountain deposit and a possible genetic link to the nearby (i.e., <5 km away) magmatic to magmatic-hydrothermal Pilot Knob ore system that comprises the massive-to-disseminated Pilot Knob Magnetite deposit and the overlying bedded and brecciated Pilot Knob Hematite deposit.

Petrographic observations, whole-rock data and the trace element and Fe isotope composition of magnetite and hematite show that the Shepherd Mountain deposit formed from at least five pulses of magmatic-hydrothermal fluids with different compositions and physicochemical parameters. Integration of the data for the Shepherd Mountain deposit with new and published data from the Pilot Knob Magnetite and Pilot Knob Hematite deposits shows that the three deposits are genetically linked through two local faults. The Ironton and Pilot Knob faults provided fluid pathways that connected the Pilot Knob Magnetite deposit to the shallower Shepherd Mountain and Pilot Knob Hematite deposits. Consequently, we argue that the Shepherd Mountain and Pilot Knob Hematite deposits are near-surface extensions of the same magmatic to hydrothermal plumbing system that formed the Pilot Knob Magnetite deposit at depth.

## 1. Introduction

The Southeast Missouri Iron Metallogenic Province in the Midcontinent region, USA occurs within an area of 35 × 115 km and hosts seven major and over twenty minor iron ore deposits/prospects that are found within early Mesoproterozoic (~1500–1440 Ma) igneous rocks of the Eastern granite-rhyolite province (Fig. 1A, B; Kisvarsanyi and Proctor, 1967; Kisvarsanyi and Kisvarsanyi, 1989; Seeger, 2000). In addition to iron ore, these deposits and prospects are also speculated to contain economically significant amounts of copper, cobalt, manganese, and rare earth elements (Kisvarsanyi and Proctor, 1967; Kisvarsanyi and Kisvarsanyi, 1989; Seeger, 2000; Day et al., 2016). In the western part of the Southeast Missouri Iron Metallogenic Province, iron ore deposits such as Pea Ridge, Kratz Spring, Bourbon, Boss, and Camels Hump, are overlain by 200–500 m thick Paleozoic sedimentary rocks. In the eastern part of the metallogenic province, i.e., in the St. Francois Mountains, deposits such as Iron Mountain, the Pilot Knob Magnetite and Hematite deposits, Shepherd Mountain, and Cedar Hill,

* Corresponding author.
*E-mail address:* locmelism@mst.edu (M. Locmelis).

https://doi.org/10.1016/j.oregeorev.2021.104633
Received 29 June 2021; Received in revised form 2 December 2021; Accepted 4 December 2021
0169-1368/© 2021

UNCORRECTED PROOF

Note: Low-resolution images were used to create this PDF. The original images will be used in the final composition.

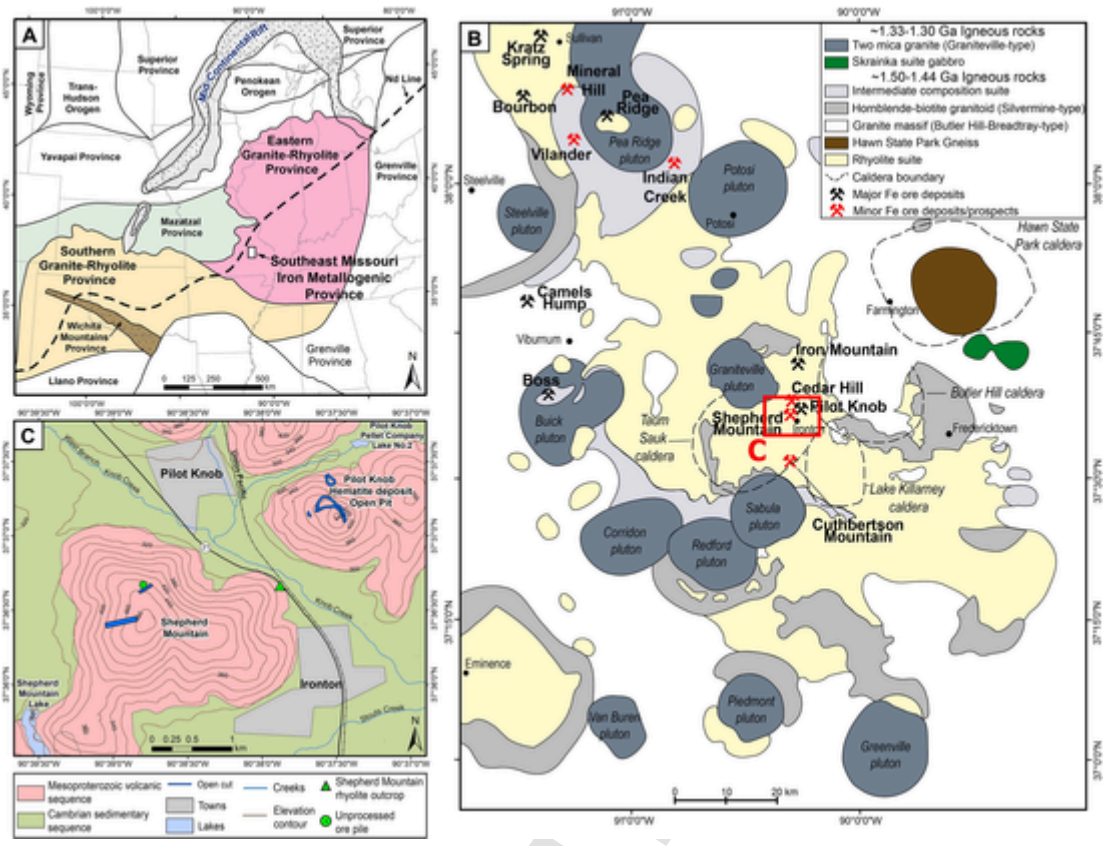


**Fig. 1.** A. The 1500–1350 Ma Granite-Rhyolite terrane in the midcontinent region of the United States with the Yavapai and Mazatzal provinces to the northwest and Llano/Grenville provinces to the southeast (modified from Van Schmus et al. (1996); Rohs and Van Schmus (2007); Bickford et al. (2015)). The white inset in 1A shows the location of the Southeast Missouri Iron Metallogenic Province. B. Simplified geological map showing igneous basement rocks of the St. Francois Mountains terrane and location of prominent iron ore deposits/prospects (modified from Day et al. (2016) and McCafferty et al. (2016)). C. Simplified geologic and topographic map showing the location of open cuts of the Shepherd Mountain and Pilot Knob Hematite deposits in Precambrian outcrops near the towns of Pilot Knob and Ironton (modified from Crane (1912)).

occur at shallower depths (<120 m) or in outcrop (Fig. 1B, C). Outcropping deposits such as Iron Mountain, the Pilot Knob Hematite deposit, Shepherd Mountain, and Cedar Hill, were mined for iron since the early 1800 s (Starkey and Seeger, 2016). Deeper deposits (≥120 m; Kratz Spring, Bourbon, Pea Ridge, Camels Hump, and the Pilot Knob Magnetite deposit) were discovered through aeromagnetic surveys in the 1940 s. Of these, only Pea Ridge (mined from 1964 to 2001) and the Pilot Knob Magnetite deposit (1965–1980) were developed into underground mining operations (Seeger, 2000).

Although the near-surface iron ore deposits were periodically mined for >150 years, most of them remain poorly studied. Pea Ridge is the most extensively studied deposit and has been proposed to be an Iron Oxide Apatite (IOA) deposit (e.g., Nold et al., 2014; Aleinikoff et al., 2016; Ayuso et al., 2016; Day et al., 2016; Harlov et al., 2016; Hofstra et al., 2016; Johnson et al., 2016; Neymark et al., 2016). Other relatively well-studied deposits are the Boss deposit, proposed to be an Iron Oxide Copper Gold-type deposit (IOCG; Seeger, 2003; Groves et al., 2010; Nold et al., 2014; Day et al., 2016), and the magmatic to magmatic-hydrothermal Pilot Knob Magnetite IOA deposit and the overlying hydrothermal Pilot Knob Hematite deposit (Nold et al., 2013; Childress et al., 2016; Tunnell et al., 2021).

It is well established that IOA and IOCG-type deposits are structurally or stratigraphically controlled (Hitzman, 2000; Williams et al., 2005; Groves et al., 2010). Several genetic models for the formation of IOA-type deposits have been proposed that are highly debated and include: (1) A magmatic model wherein an intermediate silicate melt separates into coexisting immiscible Fe-P-rich and Si-rich melts. In this model, volatiles such as F, Cl, and $H_2O$ are hypothesized to preferentially partition into the Fe-P melt, making it less dense and thus allowing it to ascend from the source magma to a shallower depth and form an IOA-type deposit (Nyström and Henríquez, 1994; Naslund et al., 2002; Tornos et al., 2017; Hou et al., 2018); (2) A magmatic-hydrothermal model in which a fluid exsolves from a magma and extracts metals from a silicate melt (Hildebrand, 1986; Jonsson et al., 2013; Westhues et al., 2017); (3) A hydrothermal or metasomatic model involving a magmatic-hydrothermal fluid (Menard, 1995; Dare et al., 2015) or a mixed ore fluid that consists of magmatic-hydrothermal and basinal brines (Rhodes and Oreskes, 1999); and (4) a combined magmatic and magmatic-hydrothermal model in which primary igneous magnetite microlites serve as nucleation sites for fluid bubbles and, therefore, are extracted to exsolving hypersaline magmatic-hydrothermal fluid along with Fe, Cu, Au, S, Cl, and P. As the fluid cools during ascent and emplacement, the igneous magnetite grows larger, sourcing metals from the fluid (Knipping et al., 2015, 2019; Ovalle et al., 2018; Simon et al., 2018).

In contrast to the different models proposed for the formation of IOA deposits, there is a growing consensus that IOCG-type deposits form primarily through hydrothermal processes, although the fluid source remains a topic of debate (Barton and Johnson, 1996; Pollard, 2006; Groves et al., 2010; Barton, 2014). Proposed fluid sources range from magmatic-hydrothermal fluids that scavenge metals from silicate melts (Pollard, 2006; Nyström et al., 2008; Rieger et al., 2010, 2012; Corriveau et al., 2016; Acosta-Góngora et al., 2018) to basinal brines that incorporate metals from the crust (Barton and Johnson, 1996; Sillitoe and Burrows, 2002; Barton, 2014). Based on the spatial and temporal associations between the IOA-IOCG deposits observed in the

UNCORRECTED

Chilean Iron Belt and the Great Bear Magmatic Zone, researchers suggested that these types of deposits form a continuum in which IOCG deposits are surface-near expressions of deeper IOA systems (Sillitoe, 2003; Knipping et al., 2015; Corriveau et al., 2016; Reich et al., 2016; Simon et al., 2018).

The iron ore deposits in the Southeast Missouri Iron Metallogenic province generally fit into the IOA/IOCG group of deposits and have been broadly compared with Kiruna-type IOA and Olympic Dam-type IOCG deposits (Kisvarsanyi and Kisvarsanyi, 1989). In addition to these IOA/IOCG-type deposits, a series of shallow vein-hosted iron oxide deposits occurs in the metallogenic province, such as the Shepherd Mountain, Shut-Ins, and Hogan deposits (Nold et al., 2014). If (and how) the shallow vein-type deposits are genetically related to the deeper IOA/IOCG-type deposits remains poorly understood although Nold et al. (2014) speculated that the vein-type deposits represent parts of a plumbing system connected to deeper magmatic iron ore deposits although currently no solid evidence exists to support such a hypothesis.

Previous studies on the ore-forming processes in the Shepherd Mountain deposit (Fig. 1B, C) have been controversial. Kisvarsanyi (1966) suggested that the deposit formed from a magmatic-hydrothermal fluid that was contemporaneous with faulting in the region. In contrast, Dudley and Nold (2001) proposed Si-poor hydrothermal fluids from which the iron oxides precipitated, although the fluid source was not specified. Consequently, the processes that formed the Shepherd Mountain deposit, and its relation to the geodynamic evolution of the Southeast Missouri Iron Metallogenic province, remain poorly understood. To constrain the genesis of the Shepherd Mountain deposit, we combine new petrographic observations with whole-rock geochemical data of iron oxide-mineralized samples and host rocks, as well as trace element and Fe isotope compositions of the iron oxide minerals. The data are used to characterize both the iron source and the processes that facilitated the formation of the vein-type mineralization. The Shepherd Mountain data are integrated with new and previously published (Tunnell et al., 2021) data from the nearby Pilot Knob deposits to reflect on a possible genetic link between the Shepherd Mountain and Pilot Knob ore system.

## 2. Geologic setting

Iron oxide deposits in Southeast Missouri occur in the Mesoproterozoic St. Francois Mountains, part of a larger Granite-Rhyolite terrane that spans from Ohio through Illinois and Missouri to Texas (Fig. 1A, B; Van Schmus et al., 1996; Rohs and Van Schmus, 2007; Bickford et al., 2015). The Granite-Rhyolite terrane is comprised of early Mesoproterozoic (~1500–1440 Ma) and middle Mesoproterozoic (1330–1300 Ma) bimodal plutonic rocks (Kisvarsanyi, 1981; Van Schmus et al., 1996; Menuge et al., 2002; Bickford et al., 2015; du Bray et al., 2021). The early Mesoproterozoic suite is broadly distributed in the eastern mid-continent and therefore is commonly referred to as the Eastern Granite-Rhyolite Province (EGRP), whereas the younger middle Mesoproterozoic suite is largely spread in the southern mid-continent, and thus is referred to as the Southern Granite-Rhyolite Province (Fig. 1A; Van Schmus et al., 1993). Overlap of the two suites occurs in the St. Francois Mountains terrane, wherein the younger suite intruded into the older rocks (e.g., Bickford et al., 2015).

The Granite-Rhyolite terrane lies between the older Mazatzal (1680–1600 Ma) province to the west and the younger Grenville (1300–900 Ma) province to the east, all of which form northeast-trending accretionary provinces that were added to the Laurentia supercontinent during an ~ 800 Myrs period of accretionary orogenesis (Karlstrom et al., 2001; Whitmeyer and Karlstrom, 2007). After an episode of tectonic inactivity between 1600 Ma and 1550 Ma, juvenile terranes and arcs resumed to accrete to the Laurentia supercontinent (Whitmeyer and Karlstrom, 2007). During the accretionary stage, the Granite-Rhyolite province has been proposed to be a product of back-arc extension, possibly caused by lithospheric delamination (Bickford et al., 2015; Day et al., 2016; Watts and Mercer, 2020; du Bray et al., 2021; Tunnell et al., 2021). The Nd-line within the Granite-Rhyolite province (Fig. 1A, delineated by Van Schmus et al. (1996), separates an older cratonic (>1550 Ma) source to the northwest from a juvenile source (<1550 Ma; possibly oceanic arc crust) to the southeast for the extensive magmatism of the early Mesoproterozoic (Bickford et al., 2015), and marks the western margin of the St. Francois Mountains terrane and the iron metallogenic province.

Iron deposits and prospects in the southeastern Missouri metallogenic province are genetically associated with the early Mesoproterozoic magmatic event from 1500 to 1440 Ma (Aleinikoff et al., 2016; Ayuso et al., 2016; Tunnell et al., 2021) and are hosted in caldera-forming volcanic and volcanoclastic sequences composed of voluminous dacite to high-silica rhyolite ignimbrites, lava flows, volcaniclastic breccias and sediments, ring fractures, and lesser amounts of basaltic andesite to dacite and trachyte volcanic and subvolcanic rocks (Kisvarsanyi, 1980, 1981; Day et al., 2016). The parental magma that is considered as the source for iron has been proposed to be derived from a subduction-modified subcontinental lithospheric mantle (Watts and Mercer, 2020; Tunnell et al., 2021) and remelting of the presumed oceanic island arc crust of calc-alkaline composition due to underplating of the mafic magma (Ayuso et al., 2016; Bickford et al., 2015; du Bray et al., 2021).

### 2.1. Geology of the Shepherd Mountain deposit

The Shepherd Mountain deposit is located southwest of the town of Pilot Knob in Precambrian outcrops on Shepherd Mountain (Fig. 1C). Previous studies of the Shepherd Mountain deposit are rare and generally limited to conference abstracts (Dudley and Nold, 2001, 2004) or short sections in regional-scale studies that primarily focus on other deposits (Kisvarsanyi, 1966; Kisvarsanyi and Kisvarsanyi, 1989; Nold et al., 2014; Day et al., 2016). Iron ore extraction at the Shepherd Mountain deposit started in 1815 and continued until the American Civil War, with 75,000 tons of iron ore produced (Crane, 1912). Ore production was restricted to two trenches (Fig. 1C) that contained magnetite ore that has been fully extracted. The northern trench is approximately 15 m wide and 140 m long, whereas the southern trench is about 20 m wide and 400 m long. The thickness of the magnetite veins varies between 1 and 7 m, pinching and swelling both along the strike and with depth. The two magnetite veins are hosted in the 1466 ± 8 Ma Shepherd Mountain rhyolite (U-Pb SHRIMP zircon age; du Bray et al., 2021). In addition to magnetite, the deposit also contains subordinate hematite and minor pyrite. The iron ore is structurally localized along two brittle fault and fracture systems, contemporaneous with the deposition of the ore (Kisvarsanyi, 1966), that strike NE 40-60° and dip steeply to the northwest at 70-80° (Day et al., 2016). The contact between the vein and host rock is relatively sharp (Fig. 2), while alteration is largely limited to an assemblage of K-feldspar + hematite + quartz in the rhyolite adjacent to the ore veins. Fragments of rhyolitic host rock entrained in the magnetite veins (Fig. 2) show evidence for K feldspar alteration with locally abundant pyrite, quartz, calcite, epidote, albite, and hematite (Day et al., 2016).

## 3. Methods

### 3.1. Sample preparation

Three rhyolitic host rock and eighteen iron oxide-mineralized samples from the Shepherd Mountain deposit were collected from unmineralized outcrops (Fig. 2A, B) and an unprocessed ore pile next to the northern mining trench (Fig. 1C, 2C, D). The ore samples were prepared as polished one-inch diameter mounts. Additionally, five thin sections were prepared: three from the Shepherd Mountain rhyolite (Fig. 2B),

UNCORRECTED PROOF

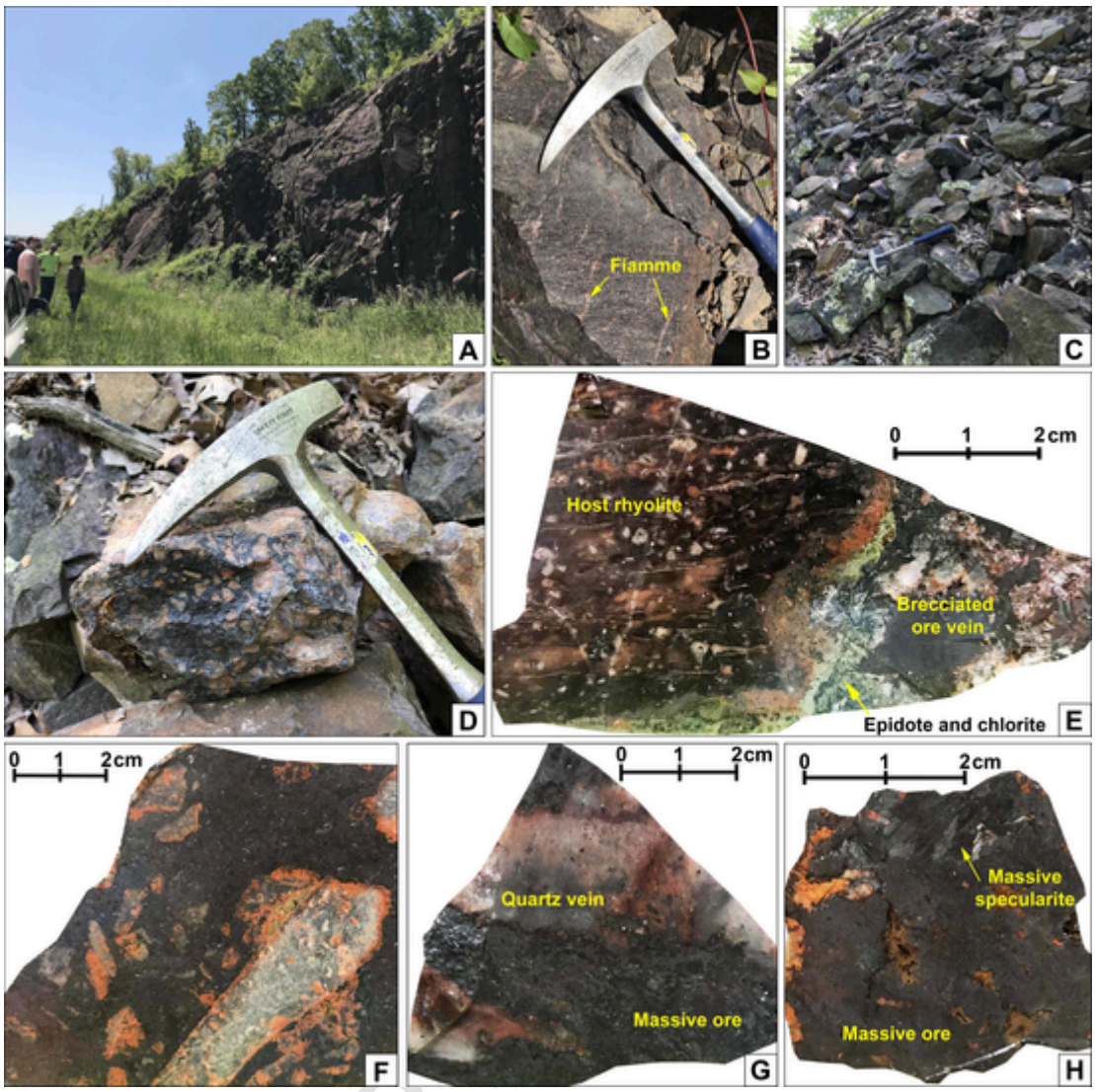


**Fig. 2.** Representative outcrop and sample photos. A. Outcrop of the Shepherd Mountain rhyolite that hosts the Shepherd Mountain iron ore deposit. The location of the outcrop is indicated by the triangle in Fig. 1C. B. Shepherd Mountain rhyolite showing fiamme textures. C. Mine tailings near the mining trench consisting of unprocessed ore and host rock samples; the location is indicated by circle in Fig. 1C. D. Breccia ore in the mine tailings. E. Fresh-cut surface of the contact between the host rock rhyolite and ore vein. F. Fresh-cut surface of the breccia ore showing K-spar + hematite alteration (pink) in fragments entrained from the volcanic host rock in the ore vein. G. Fresh cut surface showing the massive iron ore and quartz veining. H. Fresh cut surface of the massive iron ore with massive specularite.

one from the contact between ore and host rock (Fig. 2E; sample ID: SM-F11), and one from the breccia ore (Fig. 2F; Sample ID: SM-F2).

Ultra-pure two mushketovite and two magnetite concentrates (30–50 mg) were prepared from four Shepherd Mountain ore samples for iron isotope analysis. Two samples also contained specularite and were used to prepare 30–50 mg of ultra-pure specularite concentrates. All mineral concentrates were prepared in the Department of Geosciences and Geological and Petroleum Engineering (GGPE) at Missouri University of Science and Technology (Missouri S&T), Rolla, Missouri following the method described in Tunnell et al. (2021).

### 3.2. Petrographic studies

The samples were examined under reflected- and transmitted-light using a Leica DVM 6 digital microscope at Missouri S&T. A subset of samples was further characterized via scanning electron microscopy (SEM) backscattered electron (BSE) imaging and wavelength dispersive spectra (WDS) elemental x-ray mapping with a JEOL JXA-8200 electron microprobe in the Department of Earth Sciences, University of Milan (Italy).

### 3.3. Electron microprobe analysis

The major and minor element chemistry of magnetite and hematite was determined using a JEOL JXA-8200 electron microprobe equipped with wavelength and energy dispersive spectrometers (WDS and EDS) in the Department of Earth Sciences, University of Milan, Italy. The analyses were conducted in WDS mode using a 1–2 μm diameter beam with an accelerating voltage of 15 kV, a beam current of 10nA, and a counting time for each element of 30 s on peak and 10 s on background. Calibration and data reduction were done with measurements on natural and synthetic standard materials. The standards used were grossular (for Ca, Si), omphacite (Na), K-feldspar (K), olivine (Mg), fayalite (Fe), anorthite (Al), ilmenite (Ti), Cr metal (Cr), nickeline (Ni), Co metal (Co), rhodonite (Mn) and V-metal (V). Elemental concentrations were determined after applying φ(ρz) algorithm and corrections for X-ray fluorescence, absorption, atomic number (Z) and matrices, and by

UNCORRECTED

evaluating spectral interferences. Typical detection limits were 140 ppm for Ca and Al, 190 ppm for Mg, 200 ppm for Si, 220 ppm for Ti, 235 ppm for Na, 350 ppm for Mn and V, and 400 ppm for Cr, Co and Ni. Analyses were performed after verifying that $I_{xstd}/I_{std}$ was 1.00 ± 0.01 for each element, where $I_{xstd}$ was the intensity of the analyzed standard and $I_{std}$ the intensity of the same standard checked after calibration for each element. Back-scattered electron (BSE) images were collected by means of the scanning electron microscope adjoined to the probe apparatus. Elemental x-ray maps for Si, Al, and Ti were acquired in WDS mode with a beam current of 100nA and with 0.5 and 1 μm steps.

### 3.4. Laser ablation ICP-MS analysis

Trace element concentrations of iron oxides were determined using a Resonetics Resolution M−50 Excimer 193 nm laser coupled with an Agilent 7900x inductively coupled mass spectrometry (LA-ICP-MS) at LabMaTer, University du Quebec a Chicoutimi (UQAC), Canada. The analysis used a spot size of 15 μm to 50 μm with an energy of 12 mJ/pulse and a fluence of 4.8 J/cm$^2$. Thirty seconds of background were measured followed by 30–40 s of data acquisition. The following mass stations were measured: $^{23}$Na, $^{24}$Mg, $^{27}$Al, $^{29}$Si, $^{31}$P, $^{39}$K, $^{44}$Ca, $^{45}$Sc, $^{47}$Ti, $^{51}$V, $^{52}$Cr, $^{55}$Mn, $^{57}$Fe, $^{59}$Co, $^{60}$Ni, $^{63}$Cu, $^{65}$Cu, $^{66}$Zn, $^{71}$Ga, $^{74}$Ge, $^{89}$Y, $^{90}$Zr, $^{92}$Zr, $^{93}$Nb, $^{95}$Mo, $^{118}$Sn, $^{139}$La, $^{140}$Ce, $^{141}$Pr, $^{146}$Nd, $^{147}$Sm, $^{153}$Eu, $^{157}$Gd, $^{159}$Tb, $^{161}$Dy, $^{165}$Ho, $^{167}$Er, $^{169}$Tm, $^{173}$Yb, $^{175}$Lu, $^{178}$Hf, $^{181}$Ta, $^{182}$W, and $^{208}$Pb. All data were reduced using the Glitter software (Griffin et al., 2008). Elemental abundances were determined using the USGS Fe-rich glass reference material GSE-1 as a bracketing standard and Fe concentrations obtained by electron microprobe as the internal standard. The certified reference material glasses GSD (USGS glass: Jochum et al., 2007), Gprob6 (USGS-matrix artificial basalt glass), and the Ti-rich magnetite standard BC-28 (Dare et al., 2014) were used to assess the accuracy and precision of the analyses. As summarized in Online Resource ESM-1, most trace elements were determined with an accuracy of < 5% and a 2σ precision of < 10% for the GSD standard, an accuracy of < 15% and a 2σ precision of < 15% for the Gprobe6 standard. However, higher uncertainties were observed for a few elements with low concentrations in the Gprobe6 standard, whereas higher uncertainties were found in the BC-28 standards for most trace elements, as it is a natural sample from Bushveld Complex and, therefore, some elements are heterogeneously distributed within the crystal lattice (*cf.* Dare et al., 2014).

### 3.5. Iron isotope analysis

The ultra-pure mushketovite, magnetite, and specularite concentrates were dissolved in 4 ml heated ultrapure aqua regia and the solutions were dried. Iron was purified using a BioRad MP-1 anion exchange resin after drying the Fe solution following the procedure by Maréchal et al. (1999). The analysis was then performed using a Neptune multi-collector-inductively coupled plasma-mass spectrometer (MC-ICP-MS) at Pennsylvania State University, USA. The instrument setup, sample introduction, and running conditions used are described in Yesavage et al. (2016). Individual samples were measured twice at approximately 2 ppm in high-resolution mode, which generated a 13 V signal on the shoulder of the Fe peak. The instrumental mass bias was corrected for all measurements by bracketing with international IRMM-014 standard (Institute for Reference Materials and Measurements, Belgium, Taylor et al., 1992). Results are reported relative to IRMM-014 using Eq. (1):

$$\delta^{56}Fe\ (‰) = [(^{56}Fe/^{54}Fe)_{measured}/(^{56}Fe/^{54}Fe)_{IRMM\text{-}14} - 1] * 1000 \quad (1)$$

The in-house standard SRM-3126a with reported value of $\delta^{56}$Fe = 0.34‰ ± 0.1‰ 2σ (Yesavage et al., 2016) yielded an average value of $\delta^{56}$Fe = 0.29 ± 0.07‰ (n = 6). The international standard HPS-WU with reported value of $\delta^{56}$Fe = 0.60‰ ± 0.07‰ 2σ (Beard et al., 2003) yielded an average value of $\delta^{56}$Fe = 0.67 ± 0.09‰ (n = 6). All errors fall within the range of 0.1‰ 2σ of the standards.

### 3.6. Whole-rock analysis

Major, minor, and trace element whole rock analyses of host rocks and ore samples were carried out at Activation Laboratories, Ontario, Canada. Major elements were measured using X-Ray Fluorescence (XRF) analysis with detection limits of 0.001–0.01 wt%. Trace element contents were determined by open vessel multi-acid digestion followed by ICP-MS analysis (detection limits of 0.01–30 ppm). Comparison of analyzed reference materials (DNC-1, GBW 07113, TDB-1, W-2a, SY-4, and BIR-1a) with certified values show that major elements were determined with a precision of better than 7% accuracy and a 2-sigma external precision ≤ 3%. Trace elements were mostly determined with an accuracy of better than 10% and a precision of ≤ 4% (2-sigma; ESM-2).

## 4. Results

### 4.1. Petrography of the Shepherd Mountain deposit

*Volcanic host rocks:* The volcanic host rock of the Shepherd Mountain deposit is a porphyritic rhyolite containing phenocrysts of alkali feldspar, plagioclase, and devitrified fiammes (Fig. 2B). The fiammes are replaced by quartz and feldspar in a microcrystalline matrix of quartz (Fig. 3A). Alkali feldspar phenocrysts (< 2 mm long) show subhedral to anhedral textures and advanced signs of alteration to calcite and locally contain epidote and chlorite (Fig. 3B). Plagioclase phenocrysts (< 1 mm long) display subhedral to anhedral textures (Fig. 3C). Most plagioclase phenocrysts show evidence for clay alteration, while only a few phenocrysts kept their polysynthetic twinning (Fig. 3C). It is noted that the volcanic host rocks locally contain disseminated magnetite that is partially martitized (Fig. 3A, B).

*Contact Zone:* The contact between the ore veins and the volcanic host rock (Fig. 2E) is characterized by the presence of abundant calcite, epidote, chlorite, and quartz (Fig. 3D, E). In the contact zone, the host volcanic rock and its phenocrysts (e.g., plagioclase) are largely replaced by microcrystalline quartz and minor calcite (Fig. 3F). Locally, fragments of host rock that are cemented by iron oxides (Fig. 2F) within brecciated parts of ore veins show potassic and silicic alteration (Fig. 3G, H, I), while abundant epidote with minor chlorite occur between iron oxides (e.g., mushketovite, specularite) and K feldspars (Fig. 3G, I). Central portions of the fragments entrained from the host rock are characterized by silicification wherein the pre-existing minerals are replaced largely by quartz with minor calcite (Fig. 3H).

*Ore veins:* The iron ore veins consist of brecciated (Fig. 2F) and massive ores (Fig. 2G, H). Brecciated ores are characterized by elongated mushketovite, a magnetite pseudomorph after specularite, which was identified under reflected light based on its reflectance, color and lamellar-like habit (Fig. 4A, B), whereas massive ores contain euhedral to subhedral granular magnetite (Fig. 4C, D, E, H, I). Ore veins also contain lesser hematite and minor to trace amounts of pyrite. In SEM-BSE images, mushketovite exhibits patchy zoning with dark and bright domains (Fig. 4B). Granular magnetite shows oscillatory zoning patterns with alternating dark-gray and light-gray bands of varying widths and bright domains that do not show any sign of zonation (Fig. 4C, E, F, I). Hematite occurs as specularite and as martite, a pseudomorph after magnetite (Fig. 4A, C, D, H). Both mushketovite and granular magnetite are partially altered to martite (Fig. 4A-E, G, H) and martitic alteration locally shows zoning patterns with a colloform texture (Fig. 4D). Locally restricted disseminations of anhedral pyrite fill open-spaces between iron oxides (Fig. 4G).

UNCORRECTED PROOF

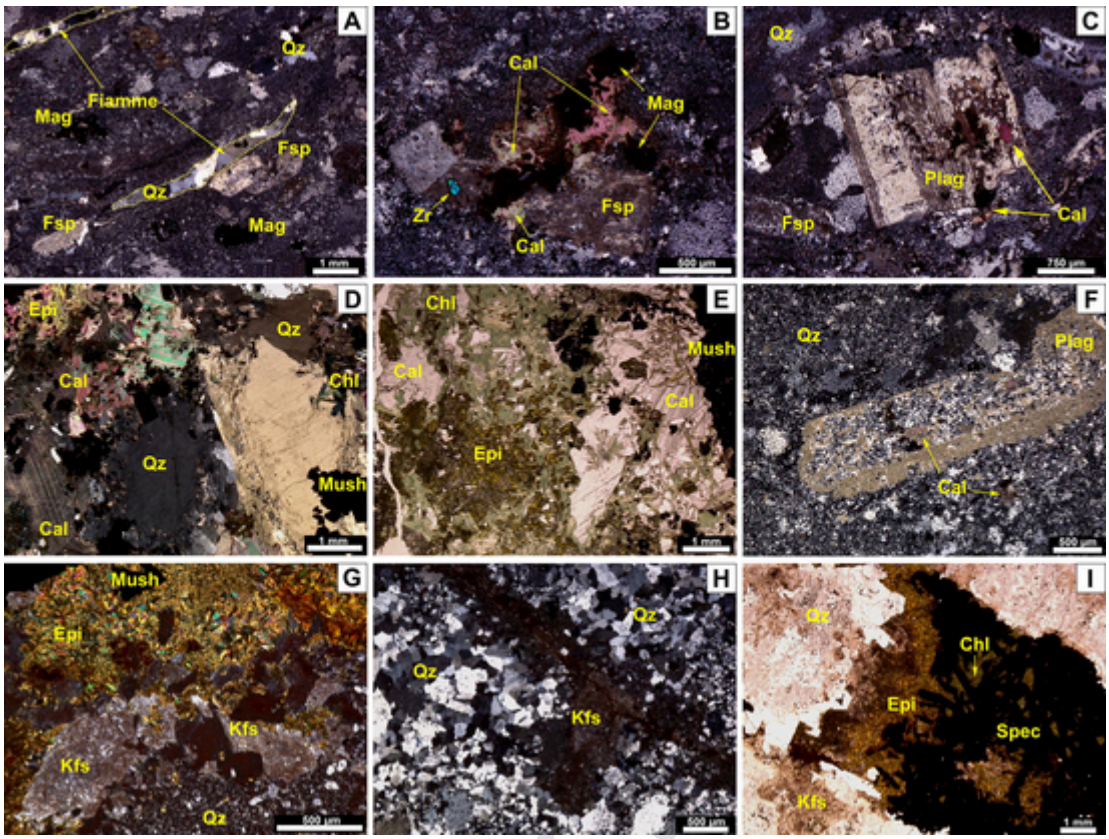


**Fig. 3.** Representative transmitted-light microscopic images of host volcanic rocks (porphyritic rhyolite) of the Shepherd Mountain deposit. A. Host rhyolite containing feldspar phenocrysts and devitrified fiammes (highlighted by dotted lines), taken from the outcrop shown as triangle in Fig. 1C (cross-polarized). B. Host rock sample showing subhedral feldspar extensively replaced by calcite (cross-polarized). C. Host rock sample showing feldspar and plagioclase phenocrysts (cross-polarized). D. Contact zone between volcanic rock and iron oxide vein (as shown in Fig. 2E) displaying abundant calcite, quartz, epidote, and chlorite (cross-polarized). E. Contact between volcanic host rock and iron oxide vein showing abundant calcite, quartz, epidote, and chlorite (plain-polarized). F. Host rock with plagioclase phenocryst extensively silicified at the contact between the host rock and ore vein (cross-polarized). G-H. Fragment of volcanic host rock within the breccia ore (as shown in Fig. 2F) displaying abundant potassic, silicic, and propylitic alterations (cross-polarized). I. Fragment of volcanic host rock within the breccia ore showing abundant potassic, silicic, and propylitic alterations (plain-polarized). Abbreviations: Qz – quartz, Fsp – feldspar, Plag – plagioclase, Cal – calcite, Epi – epidote, Chl – chlorite, Kfs – K-feldspar, Mag – magnetite, Mush – mushketovite, Spec – specularite.

### *4.2. Chemical composition of iron oxides from the Shepherd Mountain deposit*

The results of the electron microprobe analyses on iron oxides and laser ablation ICP-MS data are presented in Online Resource ESM-1. Iron oxides from the Shepherd Mountain deposit can be divided into mushketovite, high-Si magnetite, low-Si magnetite, specularite, and martite. Here, high-Si magnetite refers to magnetite with > 1 wt% $SiO_2$, as per Shiga (1988), and corresponds to darker domains of magnetite in the SEM-BSE images shown in Fig. 4C, E, F, and I. In contrast, low-Si magnetite has < 1 wt% $SiO_2$ and corresponds to brighter domains of magnetite in BSE images (Fig. 4E, F, I). Elemental X-ray maps in Fig. 5 display clearly distinct bands of Si and, to a lesser extent, Al. Darker domains in the BSE images correspond to the elevated Si contents with alternating bands within the oscillatory zonation. Along with Si, Al and Ti appear to be slightly elevated in the darker domains (although less so than Si). However, in some cases, Ti does not change correspondingly with either Si or Al such as shown in Fig. 5B; instead Ti shows a different chemical behavior during magnetite growth.

*Magnetite:* Electron microprobe analyses show that high-Si magnetite, with > 1 wt% $SiO_2$, contains between 67.6 and 71.1 wt% Fe (average of 69.3 wt%) and 0.5–2.4 wt% Si, while low-Si magnetite, with < 1 wt% $SiO_2$, is characterized by 71.2–74.5 wt% of Fe (average of 72.8 wt%) and 0.01–0.5 wt% Si (ESM-1). Laser ablation-ICP-MS analyses show that the high-Si magnetite contains between 660 and 12400 ppm Al, 390 to 5000 ppm Mg, and 1500 to 9200 ppm Ca. In contrast, low-Si magnetite contains between 140 and 2000 ppm Al, 12 to 840 ppm Mg, and 25 to 2200 ppm Ca. Low-Si magnetite is further characterized by lower contents of high field strength elements (HFSE: Ti, Nb, and Sc) (Fig. 6A); typically between 25 and 340 ppm Ti, 0.004–0.73 ppm Nb, and 0.1 – 3.7 ppm Sc, whereas high-Si magnetite contains between 14 and 550 ppm Ti, 0.05–1.6 ppm Nb, and 3–40 ppm Sc. Conversely, both high-Si and low-Si magnetite grains have similar concentrations of first-row transition elements (FRTE), i.e., between 420 and 1900 ppm Mn, 45–140 ppm Co, and 4–17 ppm Ni, except for Cr and V. Chromium and V concentrations vary from 0.4 to 22 ppm Cr and 1 to 66 ppm V, respectively, in high-Si magnetite, whereas they range from 0.3 to 2.1 ppm Cr and 10 to 110 ppm V in low-Si magnetite (Fig. 6A, ESM-1). With regards to granitophile-group elements (Pb, W, Sn, Mo), high-Si magnetite is relatively more enriched as it contains between 0.3 and 8.4 ppm Pb, 7.7–68 ppm W, 0.8–5.6 ppm Sn, and 0.2–122 ppm Mo. Low-Si magnetite grains are characterized by between 0.01 and 4.4 ppm Pb, 0.01–48 ppm W, 0.1 – 1.2 ppm Sn, and 0.03 – 7.8 ppm Mo (Fig. 6A, ESM-1).

*Mushketovite:* Electron microprobe analyses show that mushketovite contains between 72.6 and 73.9 wt% Fe (average of 73.3 wt% Fe) and 0.01–0.4 wt% Si (Fig. 6B; ESM-1). Laser ablation-ICP-MS analyses show that mushketovite contains between 370 and 1550 ppm Al, 110 – 720 ppm Mg, and 1180 – 1450 ppm Ca. With regards to HFSE, mushketovite contains between 35 and 90 ppm Ti, 0.05 and 0.7 ppm Nb, and 1.8 and 4.8 ppm Sc. In terms of FRTE, mushketovite contains

UNCORRECTED PROOF

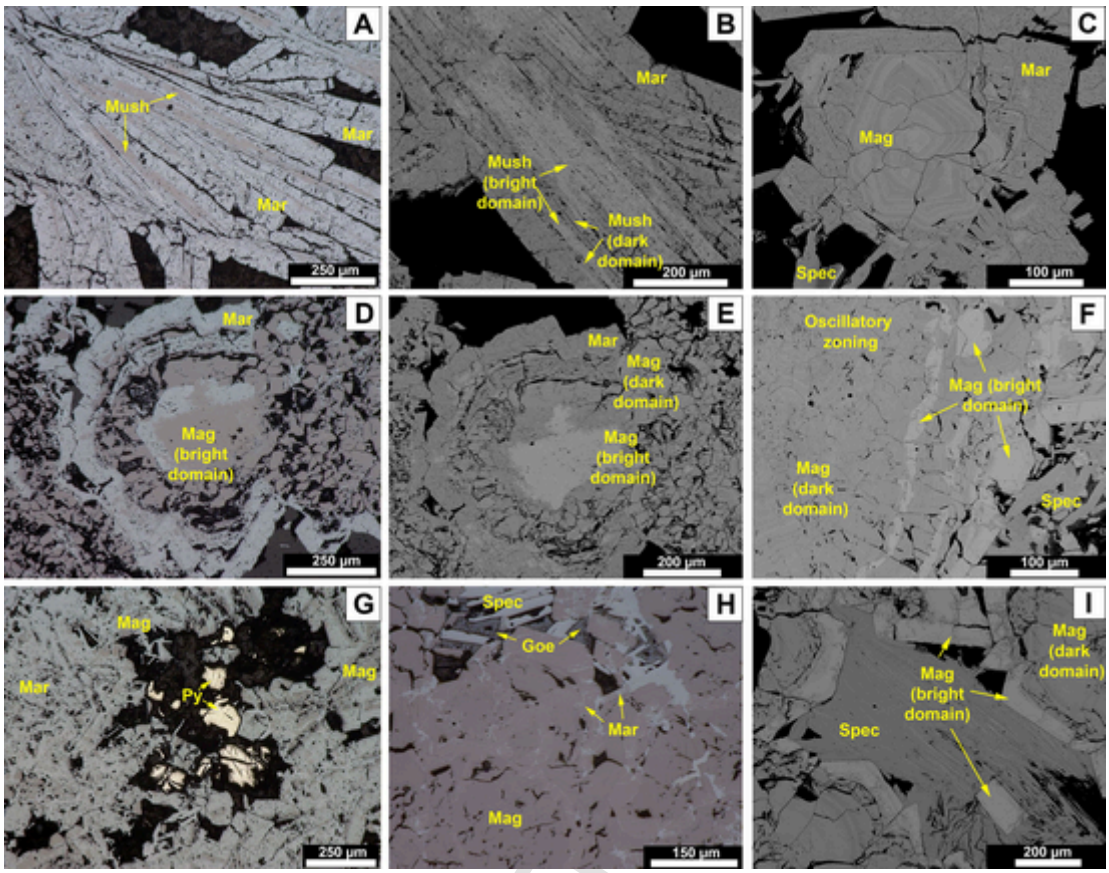


**Fig. 4.** Representative photomicrographs and BSE images of ore samples from the Shepherd Mountain deposit. A. Mushketovite with martitization under reflected-light. B. Mushketovite displaying bright and dark domains (BSE image). C. Oscillatory zoned magnetite with alternating bright and dark domains and martitization along the edges (BSE image). D. Granular magnetite with zoned martitization under reflected-light. E. BSE image of the grain from 4d showing bright and dark domains of magnetite. F. Oscillatory zoned massive magnetite with bright domains and specularite (BSE image). G. Matrix magnetite/mushketovite with martitization and anhedral pyrite under reflected-light. H. Massive magnetite with minor martite replacing magnetite selectively along $d_{111}$ planes and open space-filling specularite and goethite (reflected-light image). I. Granular magnetite dominated by bright domain (BSE image). Abbreviations: Mar – martite, Mag – magnetite, Mush – mushketovite, Spec – specularite, Goe - goethite.

between 6 and 37 ppm V, 4.2 ppm Cr (detected in only one analysis), 720–1000 ppm Mn, 64–69 ppm Co, and 6–10 ppm Ni. Additionally, it contains 3.8 to 8 ppm Pb, 980 to 3450 ppm W, 0.7 to 26.5 ppm Sn, and 10.7 to 34 ppm Mo.

*Specularite:* Electron microprobe analyses show that specularite contains between 69.2 and 71.4 wt% Fe (average of 70.4 wt% Fe) and 0.004–0.2 wt% Si (Fig. 6B; ESM-1). Laser ablation-ICP-MS analyses show that specularite contains between 110 and 3400 ppm Al, 2–1075 ppm Mg, and 6 – 620 ppm Ca. In terms of HFSE, specularite contains between 130 and 4200 ppm Ti, 0.2–10 ppm Nb, and 1.4–147 ppm Sc (Fig. 6b). Among the FRTE, V contents in specularite vary between 16 and 140 ppm V, 0.2–5.3 ppm Cr, 36–810 ppm Mn, 0.1–23 ppm Co, and 0.03–10 ppm Ni. With respect to granitophile-group elements, specularite contains between 0.4 and 7 ppm Pb, 22–2800 ppm W, 0.4–17 ppm Mo, and 2–135 ppm Sn (Fig. 6B).

*Martite:* Electron microprobe analyses show that martite contains between 68.1 and 71.5 wt% Fe and 0.02–0.5 wt% Si. Laser ablation-ICP-MS data show that martite contains between 820 and 1700 ppm Al, 12–450 ppm Mg, 32 – 1550 ppm Ca. Among the HFSE, martite contains 42–280 ppm Ti, 0.02 – 0.2 ppm Nb, and 1.3–4.4 ppm Sc (Fig. 6B). Additionally, martite contains between 30 and 86 ppm V, 0.6–2.0 ppm Cr, 550–1430 ppm Mn, 56–66 ppm Co, and 11–14 ppm Ni (Fig. 6B). In terms of granitophile group elements, martite contains between 0.1 and 218 ppm W, 0.1 – 0.6 ppm Sn while Pb is between 1.4 and 7.4 ppm and Mo is between 0.1 and 6.8 ppm, which are similar to that within specularite (Fig. 6B).

### 4.3. Chemical composition of iron oxides from the Pilot Knob magnetite deposit

In addition to the new mineral data from Shepherd Mountain, this study also presents the first trace element data for magnetite, martite, and hematite from the PKM deposit obtained by laser ablation ICP-MS (Fig. 6, ESM-1) that complements a single LA-ICP-MS analysis reported by Huang et al. (2019). It is noted that the trace element composition of martite and hematite was only measured on a sample from shallow depth (~177 m; sample ID: PKM-1098–580) as samples from deeper portions only contained very minor hematite and martite. The trace element data are integrated with Fe contents obtained by electron microprobe from Tunnell et al. (2021).

*Magnetite* from the PKM deposit contains between 70.8 and 74.0 wt% Fe (average of 73.1 wt% Fe) and between < 140 ppm and 6600 ppm Si. It is noted that, in contrast to the Shepherd Mountain deposit, no high-Si magnetite was observed in the PKM deposit. Laser ablation-ICP-MS data show that magnetite contains between 20 and 8900 ppm Al, 3.4–1040 ppm Mg, and 5 – 1140 ppm Ca (Fig. 6A, ESM-1). In terms of HFSE, PKM magnetite contains between 70 and 3500 ppm Ti, 0.01–5 ppm Nb, and 0.1–7 ppm Sc (Fig. 6A, ESM-1). Among the FRTE, the PKM magnetite contains between 36 and 340 ppm V, 0.2–56 ppm Cr, 340–1850 ppm Mn, 10–67 ppm Co, and 5–40 ppm Ni (Fig. 6A, ESM-1). With respect to granitophile elements, magnetite contains between 0.004 and 2.4 ppm Pb, 0.01–124 ppm W, 0.14–7 ppm Sn, and 0.03–57 ppm Mo (Fig. 6A, ESM-1).

UNCORRECTED

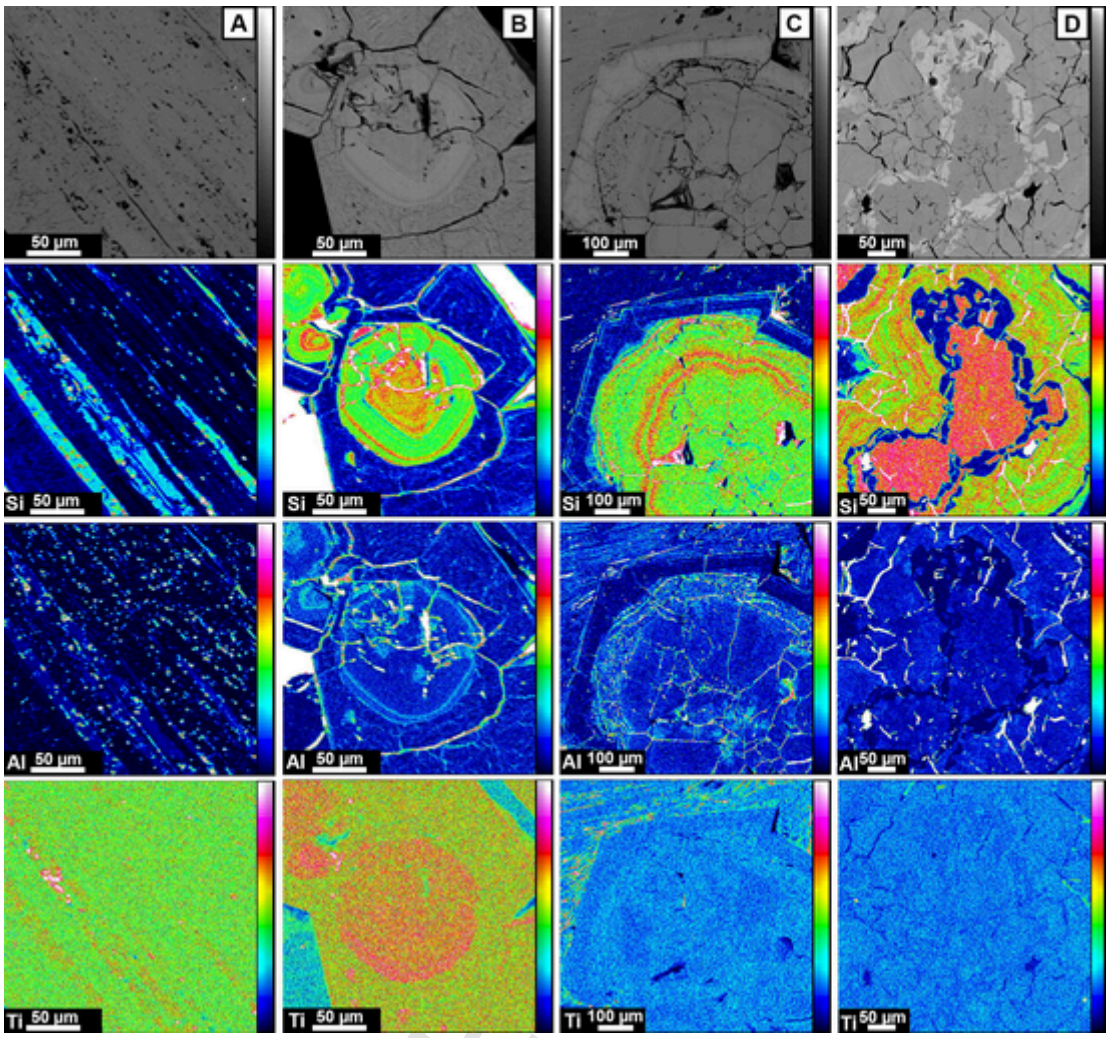


**Fig. 5.** WDS X-ray elemental maps of selected trace elements for mushketovite (A) and magnetite (B, C, D) from the Shepherd Mountain deposit.

*Hematite* from the PKM deposit contains between 66.0 and 71.1 wt% Fe (average of 67.5 wt% Fe) and < 140 ppm Si. Furthermore, hematite contains between 1130 and 2900 ppm Al, 100–250 ppm Mg, 31–73 ppm Ca, 110–150 ppm V, 4 – 10 ppm Cr, 32–170 ppm Mn, 0.2–0.6 ppm Co, and 0.1–1 ppm Ni (Fig. 6C, ESM-1). Additionally, hematite contains between 25,000 – 48,000 ppm Ti, 57–86 ppm Nb, 57–94 ppm Sc, 0.1 – 1.6 ppm Pb, 0.8 – 9 ppm W, 55–94 ppm Sn, and 0.3–2.6 ppm Mo (Fig. 6C, ESM-1).

*Martite* from the PKM deposit contains between 70.6 and 71.8 wt% Fe (average of 71.2 wt% Fe), <140 ppm Si, 125–1650 ppm Al, 24–210 ppm Mg, and 6–33 ppm Ca (Fig. 6C, ESM-1). Martite also contains between 83 and 106 ppm V, 2–5.6 ppm Cr, 130–245 ppm Mn, 1.5–3.8 ppm Co, and 6.6–20 ppm Ni. With regards to HFSE, martite contains between 380 and 620 ppm Ti, 0.1–2 ppm Nb, and 7.5–10 ppm Sc (Fig. 6C, ESM-1). Additionally, martite contains 0.5–1.8 ppm Sn and 0.01–0.2 ppm Mo. Lead and W concentrations in martite are between 0.1 and 1.6 ppm and 0.8 and 9 ppm, respectively, similar to those determined in hematite.

### 4.4. Stable Fe isotope chemistry

The stable Fe isotope ratios of two mushketovite, two magnetite, and two specularite samples from the Shepherd Mountain deposit are given in Table. 1 and illustrated in Fig. 7. The average $\delta^{56}$Fe values for mushketovite, magnetite, and specularite are −0.35‰, −0.21‰, and −0.13‰, respectively.

### 4.5. Whole-rock geochemistry

New whole-rock data for iron oxide-mineralized samples from the Shepherd Mountain deposit and their volcanic host rocks are integrated with publicly available USGS whole-rock data that have been compiled by Day et al. (2017). All new whole-rock data discussed here are presented in ESM-2.

*Volcanic host rocks:* The volcanic host rocks of the Shepherd Mountain deposit are classified as rhyolite and dacite based on the immobile element diagram of Nb/Y vs. Zr/Ti (Pearce, 1996) that is used to eliminate alteration effects (Fig. 8A). Consequently, the host rocks of the Shepherd Mountain deposit are similar to the host rocks of the PKM deposit (Fig. 8A). The rhyolites and dacites plot as volcanic arc granite on Y vs. Nb diagram (Fig. 8B; Pearce et al., 1984), but approximately half the samples display A-type signatures while the others show I & S type granite on Ga/Al*$10^4$ vs. Zr diagram (Fig. 8C; Whalen et al., 1987)The host rocks of the Pilot Knob Magnetite deposit mostly plot as within-plate A-type granites. On the $(Y/Nb)_N$ vs. $(Th/Nb)_N$ diagram, the host volcanic rocks fall within the field of A2 type granite that indicates emplacement at a convergent boundary (Fig. 8D; Moreno et al., 2014).

C1 chondrite-normalized rare earth element (REE) patterns of the host rhyolites of the Shepherd Mountain deposit display a strong fractionation between light rare earth elements (LREE) and heavy rare earth elements (HREE) with a flat trend from medium REE (MREE) to HREE, similar to the host rhyolites of the PKM deposit (Fig. 9A). How-

UNCORRECTED

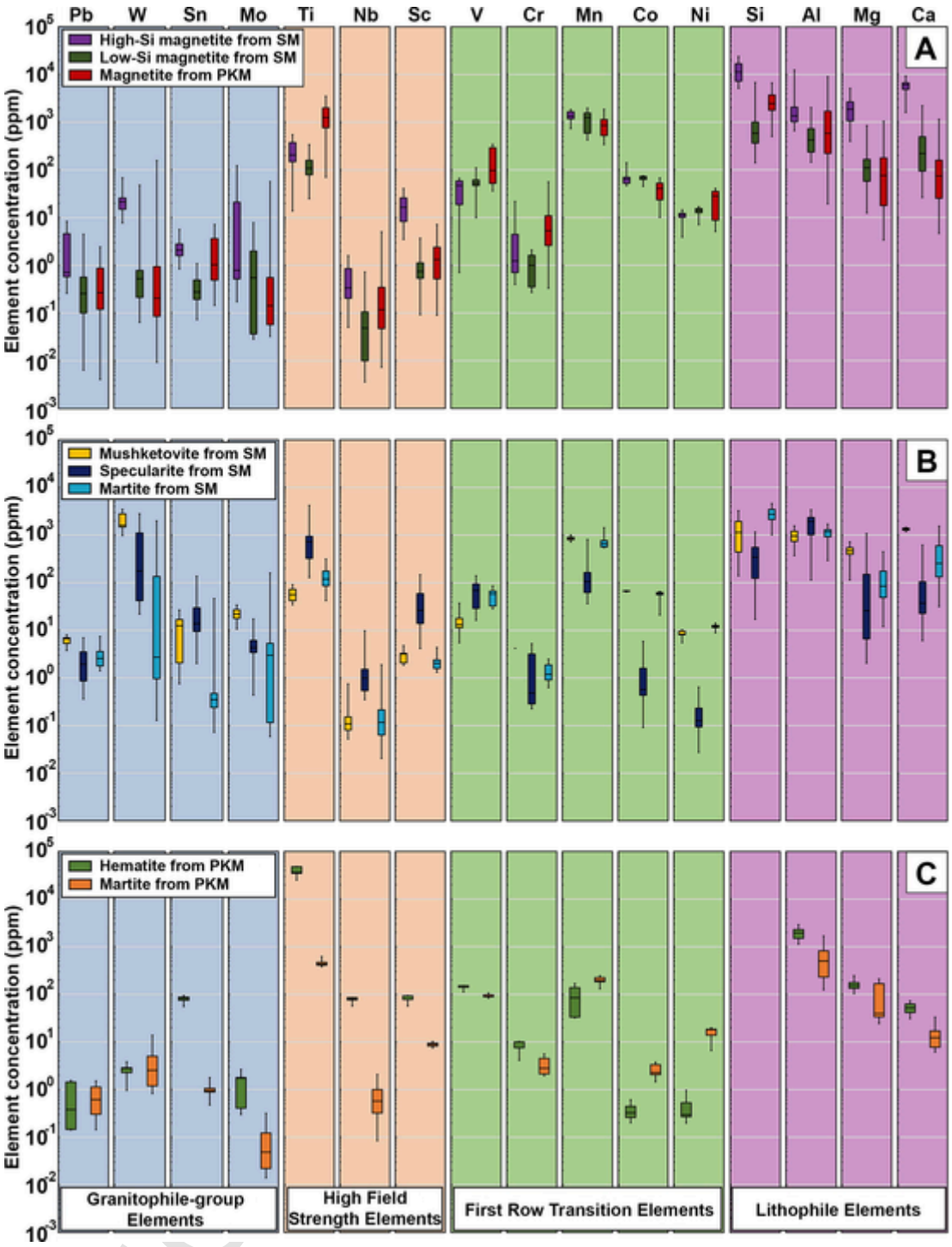


**Fig. 6.** Box and whisker plots for selected EMPA and LA-ICP-MS elemental abundances for: A. magnetite from both the Shepherd Mountain (SM) and Pilot Knob Magnetite (PKM) deposits; B. mushketovite, specularite and martite from the Shepherd Mountain deposit; C. hematite and martite from the Pilot Knob Magnetite deposit. Note: Si contents in hematite and martite from PKM are below detection limit (<140 ppm). Boxes display the 25th and 75th percentiles, and whiskers extend to the minimum and maximum values. Short line within the box indicates the median value.

ever, the host rocks of the Shepherd Mountain deposit show a pronounced Eu negative anomaly ($Eu_N/Eu_N^*$ = 0.4 – 0.7), while the PKM host rocks display only a slight and/or no negative Eu anomaly ($Eu_N/Eu_N^*$ = 0.6 – 0.9; Fig. 9A; ESM-2). Bulk Silicate Earth (BSE)-normalized multi-element spider diagrams for both the Shepherd Mountain and Pilot Knob deposits show negative anomalies for Nb, Ta, Sr and Sc, and enrichments in Th, La, Ce, Pb, and Nd (Fig. 9B).

*Ore samples:* Magnetite- and hematite-mineralized whole-rock ore samples from the Shepherd Mountain deposit contain between 47 wt% and 97 wt% $Fe_2O_3$ (ESM-2). C1 chondrite normalized REE patterns show a decreasing trend from La to Lu with a wide range of variability with respect to LREE, whereas less variability is observed in MREE and HREE (Fig. 10A). The PKM ore samples display a similar decreasing trend from LREE to MREE, but a flat trend from MREE to HREE. Pronounced negative Eu anomalies ($Eu_N/Eu_N^*$ = 0.3–0.7) are observed for the Shepherd Mountain mineralized samples, while the PKM ore samples show variable Eu anomalies ($Eu_N/Eu_N^*$ = 0.7 – 1.6; Fig. 10A). Bulk silicate Earth (BSE)-normalized multi-element spidergrams show

**Table 1**
Summary of iron isotope analyses of mushketovite, magnetite, and specularite from the Shepherd Mountain deposit.

| Location | Sample ID | Mineral | Average $\delta^{56}$Fe (‰) |
|---|---|---|---|
| Shepherd Mountain | SM-F1 | Mushketovite | −0.14 |
| | SM-F11 | Mushketovite | −0.55 |
| | SM-F8 | Magnetite | −0.15 |
| | SM-F17 | Magnetite | −0.26 |
| | SM-F11 | Specularite | −0.07 |
| | SM-F17 | Specularite | −0.19 |

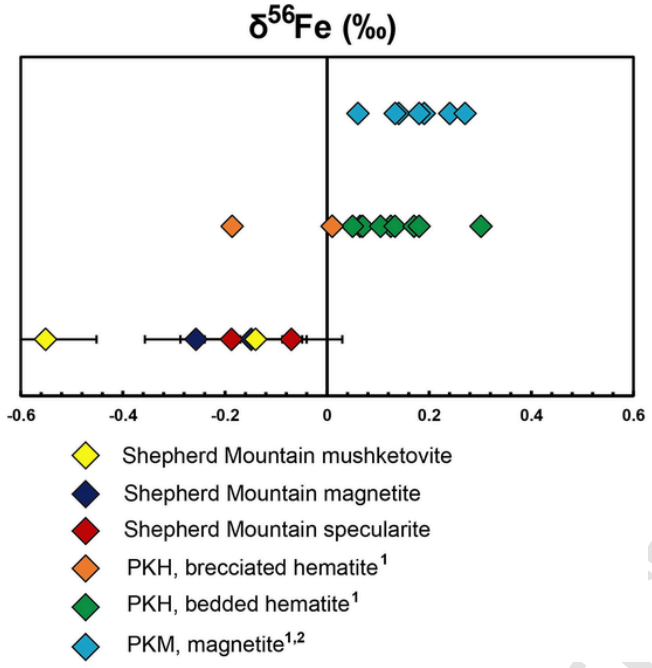


**Fig. 7.** The stable Fe isotope compositions of mushketovite, magnetite, and specularite from the Shepherd Mountain deposit. The $\delta^{56}$Fe values of magnetite and hematite from the PKM and PKH deposits, respectively, are included for comparison. The reported values are an average of two measurements. Error bars indicate the conservative errors of the variations of the standard. Data source: 1 = Tunnell et al. (2021), 2 = Childress et al. (2016).

negative anomalies for Nb, Ta, Sr, Ti, and Al, while the PKM ore samples display similar negative peaks for Nb, Ta, and even a stronger Sr depletion (Fig. 10B). The Shepherd Mountain ore samples have higher concentrations of Sc, but lower concentrations of Ti and Al compared to the PKM ores (Fig. 10B).

## 5. Discussion

Although the Shepherd Mountain iron ore deposit was previously mined from 1815 to 1865, studies on its genesis are rare and limited to conference abstracts (Dudley and Nold, 2001, 2004) and short paragraphs in papers that otherwise focus on different deposits and/or regional geologic aspects (Kisvarsanyi, 1966; Kisvarsanyi and Kisvarsanyi, 1989; Nold et al., 2014; Day et al., 2016). Previous studies proposed either a (i) magmatic-hydrothermal deposition of ore controlled by contemporaneous fault systems (Kisvarsanyi, 1966); or (ii) a hydrothermal origin related to infiltration by a Si-poor fluid (Dudley and Nold, 2001). However, to the best of our knowledge, there are no published studies that identify the fluid source(s) and quantitatively discuss how the Shepherd Mountain deposit is genetically related to the nearby magmatic-hydrothermal Pilot Knob ore system. Although Nold et al. (2014) hypothesized that vein-type deposits in southeast Missouri represent part of plumbing system where they form from ascending Fe-bearing ore fluids from magmatic deposits at depth, this hypothesis remained untested until this study. Furthermore, previous studies did not fully unravel the order of mineralizing events in the Shepherd Mountain deposit that are indicated by the different ore minerals and textures. Here, we investigate the following aspects:

(i) The order of events that formed the different ore textures which we propose in Fig. 11.
(ii) The genesis of the Shepherd Mountain deposit and whether it is of magmatic-hydrothermal or hydrothermal origin.
(iii) A possible genetic link between the Shepherd Mountain and Pilot Knob deposits which we propose in the illustration shown as Fig. 12.

### 5.1. Ore-genetic sequence of the Shepherd Mountain deposit

#### 5.1.1. Origin of the breccia ores

At Shepherd Mountain, mushketovite occurs in brecciated samples where it forms a cementing groundmass between individual clasts derived from the host rocks (Fig. 2F). Mushketovite is a pseudomorphic replacement of specularite by magnetite that forms under reducing conditions commonly below the hematite-magnetite buffer (Ohmoto, 2003; Mucke and Cabral, 2005). Although the veins are mined out and structural relationships are no longer discernable in the field, we interpret that the breccias represent samples close to the wall rock contact based on the ubiquity of host rock clasts as illustrated in Fig. 12A. Conversely, the granular to massive magnetite ores do not contain any host rock fragments (Fig. 2G, H) and thus are speculated to occur in the central portions of the veins (Fig. 12B). Based on these observations, we argue that the brecciated ores formed at an early stage of the ore-genetic sequence at Shepherd Mountain when an Fe-rich hydrothermal fluid infiltrated the volcanic host rocks and created veins that entrained clasts from the wall rock. The clasts were cemented by early specularite that precipitated from a hydrothermal fluid (Fig. 11); the temperature of this hydrothermal fluid is constrained by the formation temperature of specularite, i.e., 100 °C to 460 °C (e.g., Catling and Moore, 2003; Cabral and Rosière, 2013; Childress et al., 2020). Our model for the formation of the brecciated ore is consistent with the observations by Kisvarsanyi (1966) who proposed that the iron oxides were deposited contemporaneously with the fault systems resulting in the breccia ores. It is noted that, at this stage, specularite, with its characteristic needle-like habit, was likely the first iron oxide mineral to precipitate from the oxidized fluid, but subsequently was reduced to mushketovite during a later pulse of hotter ore fluid and/or drop in a redox state (Fig. 11). Similar reductions of early specularite to later mushketovite are common in iron ore systems such as IOCG (e.g., Marschik and Fontboté, 2001; De Haller and Fontboté, 2009; Rieger et al., 2010; Hu et al., 2020a) and skarn deposits (e.g., Boni et al., 1990; Dünkel, 2002; Ciobanu and Cook, 2004; Prendergast et al., 2005) and are generally attributed to magmatic-hydrothermal processes.

The mushketovite at Shepherd Mountain shows patchy zoning patterns with dark and bright domains wherein the dark domains are characterized by elevated Si, Ca, and Al while the bright domains contain negligible amount of these elements based on x-ray mapping and EMPA results (Fig. 4B, 5A; ESM-1). The dark mushketovite domains with elevated Si, Al, and Ca contents overprint the bright domains (Fig. 4B, 5A); the overprinting might have been contemporaneous with the later-stage formation of high-Si granular magnetite in the central portion of the veins as further discussed in the next section, similar to processes observed for the Mina Justa IOCG deposit, Peru (Hu et al., 2020b).

The alteration assemblage in the brecciated ores at Shepherd Mountain gives insight into the temperature of the early specularite forming hydrothermal event. The breccias are characterized by potassic (K-feldspar) alteration and notably do not show any sign of sodic (albite) alteration. The potassic alteration is closely associated with Fe metaso-

UNCORRECTED PROOF

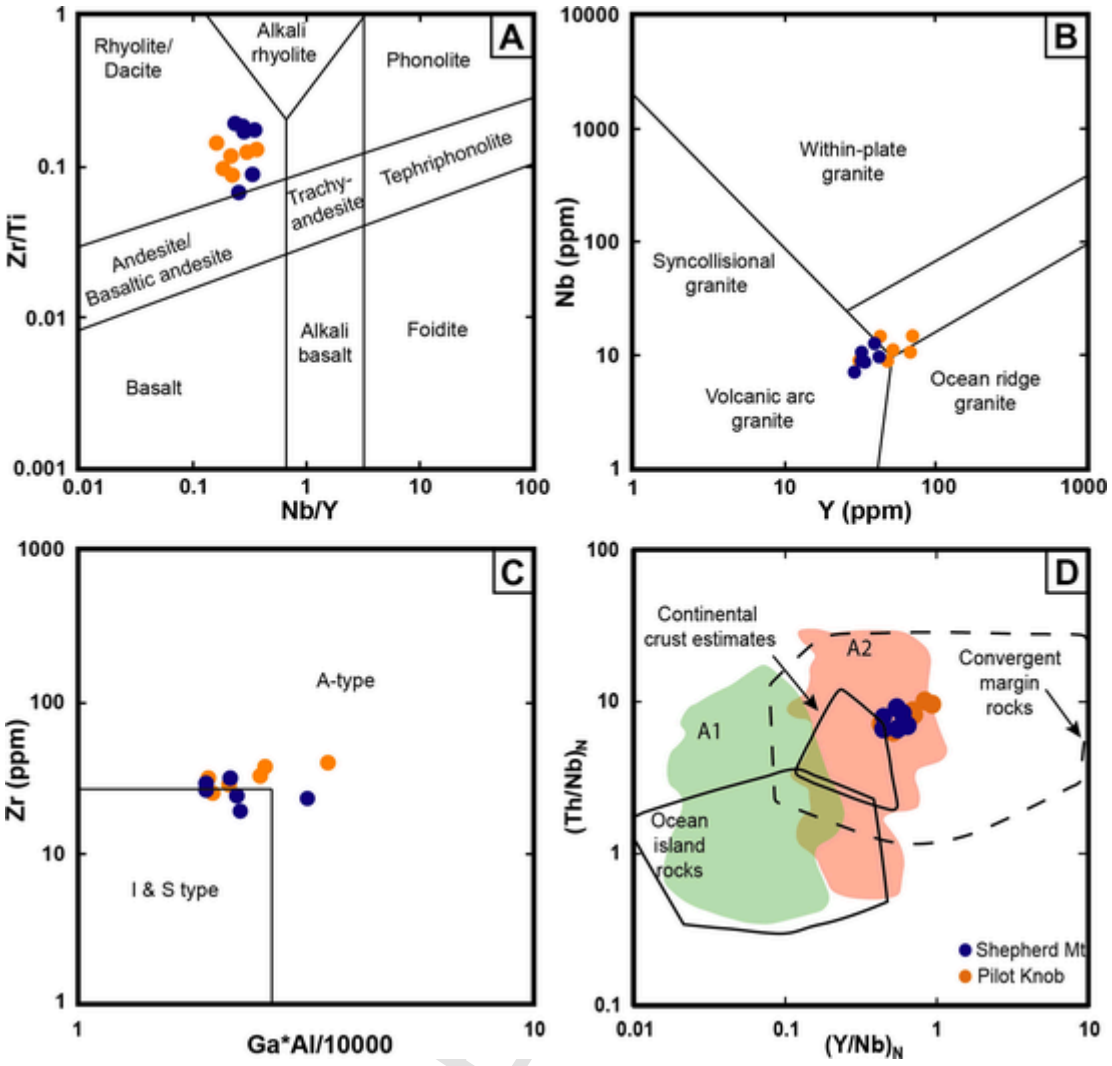


**Fig. 8.** A. Nb/Y vs. Zr/Ti classification diagram (after Pearce 1996); B. Y vs. Nb tectonic discrimination diagram (after Pearce et al., 1984); C. Ga/Al*$10^4$ vs. Zr diagram for discriminating between I&S-type and A-type granites (after Whalen et al., 1987); D. $(Y/Nb)_N$ vs. $(Th/Nb)_N$ diagram for the rhyolitic rocks. The fields of A1 and A2 granites, along with other compositional fields, are drawn after Moreno et al. (2014). Values are normalized to the Bulk Silicate Earth after McDonough and Sun (1995). The figures also include publicly available USGS whole-rock data (sample IDs: MO14_27C and MO14_031; data Source: Day et al. (2017)).

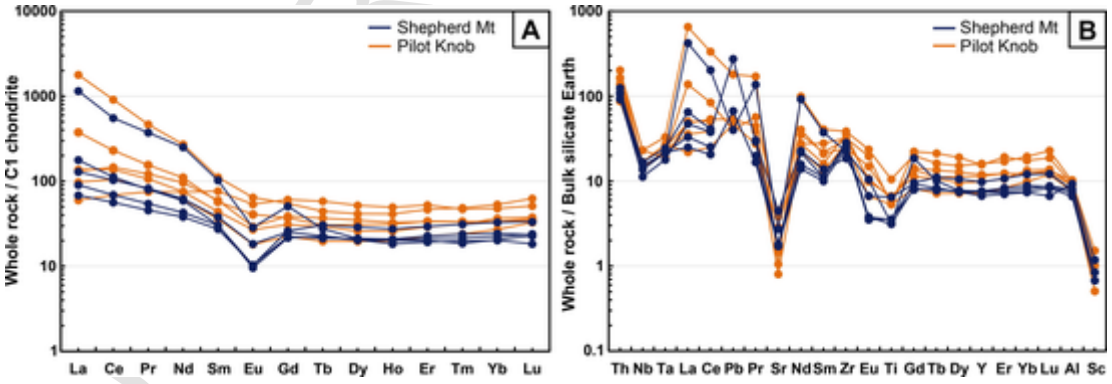


**Fig. 9.** A. C1 chondrite-normalized REE patterns for the rhyolitic host rocks of the Shepherd Mountain and Pilot Knob Magnetite deposits; B. Bulk Silicate Earth-normalized multi-element spider diagrams for the rhyolitic host rocks of the Shepherd Mountain and Pilot Knob Magnetite deposits. Normalization values for both plots are from McDonough and Sun (1995). The figures also include publicly available USGS whole-rock data (sample IDs: MO14_27C and MO14_031; data Source: Day et al. (2017)).

matism (as implied by the early specularite formation) and silicification which generally records cooling of high temperature saline fluids in the $H_2O$-NaCl-KCl-$FeCl_2$ system degassed from a magma at temperatures between 250 and 400 °C (Giggenbach, 1984; De Haller and Fontboté, 2009; Williams et al., 2005; Barton, 2014). Consequently, we argue that the early specularite at Shepherd Mountain formed from a saline hydrothermal fluid at a temperature between 250 and 400 °C. Later infiltration by a hotter magmatic-hydrothermal fluid (>400 °C as discussed

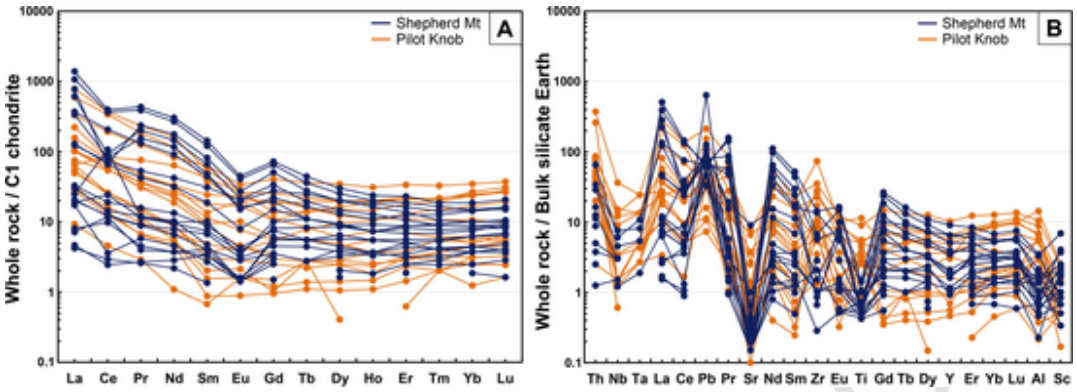


**Fig. 10.** A. C1 chondrite-normalized REE patterns for iron oxide-mineralized samples from the Shepherd Mountain and Pilot Knob Magnetite deposits; B. Bulk Silicate Earth-normalized multi-element spider diagrams. Normalization values for both plots are from McDonough and Sun (1995). The figures also include publicly available USGS whole-rock data (sample ID: MO14_14A; data Source: Day et al. (2017)).

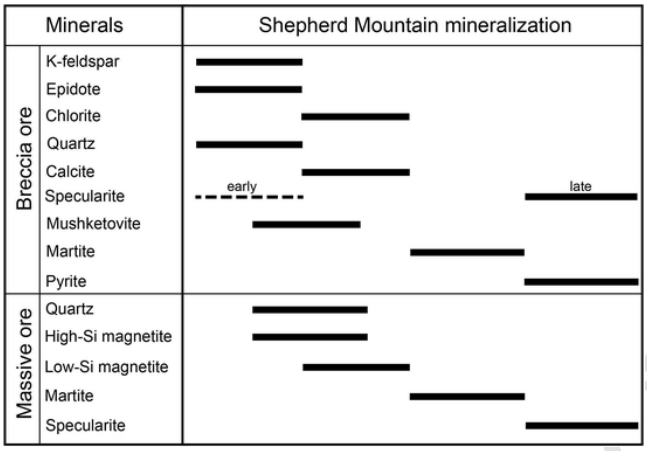


**Fig. 11.** Mineralization sequence for the Shepherd Mountain vein-type deposit.

below) triggered mushketovitization due to a decrease in a redox state below the hematite-magnetite buffer.

*5.1.2. Origin of the massive magnetite ores: Textural and compositional characteristics of high-Si vs. low-Si magnetite*

The texture and trace element chemistry of magnetite and its compositional variations can be useful in constraining the ore-forming environments and discriminating between different styles of mineralization (Dupuis and Beaudoin, 2011; Dare et al., 2012, 2014; Nadoll et al., 2014). At Shepherd Mountain, two different types of granular magnetite exist that allow us to better constrain the massive ore forming events after the early formation of specularite/mushketovite in the brecciated contact ore. One type of granular magnetite displays distinct oscillatory zoned patterns (Fig. 4C, E, F), whereas the second type is largely homogenous (Fig. 4E, F, I). The oscillatory magnetite is notably darker in BSE images when compared to the homogenous magnetite (*cf.* Figs. 4, 5). Similar oscillatory zonation patterns, typical of Si-rich magnetite, are observed in several IOA and IOCG deposits (e.g., El Laco, El Romeral, Sossego, Salobo, Candelaria, and Los Colorados), and were shown to reflect rapid crystal growth from a compositionally fluctuating fluid rather than solely being related to variation in temperature and oxygen fugacity (Shore and Fowler, 1996; Reich et al., 2013; Dare et al., 2015; Deditius et al., 2018; Huang and Beaudoin, 2019). Consequently, the oscillatory zonation observed in the darker domains of magnetite at Shepherd Mountain likely implies that the magnetite grew rapidly from a compositionally fluctuating fluid.

It is noted that the oscillatory zoned magnetite has significantly higher concentrations of lithophile elements (i.e., Si, Al, Ca, and Mg) than the homogeneous low-Si magnetite that, as a consequence, is more Fe rich and therefore brighter in BSE images (Figs. 4, 5, 6, 13A). High Si and Ca contents in magnetite are commonly attributed to magnetite precipitation from hydrothermal fluids (Shimazaki, 1998; Dare et al., 2014; Nadoll et al., 2014) because lithophile elements such as Si and Ca preferentially partition into silicates in evolved magmatic systems due to the low partitioning coefficients of Si ($D_{Si}$ = 0.0017) and Ca ($D_{Ca}$ = 0.035) into magnetite (Dare et al., 2012). Accordingly, the elevated Si + Ca contents of the oscillatory zoned magnetite observed here (7,200–32,000 ppm Si + Ca) are indicative of hydrothermal magnetite, which is consistent with the indication from oscillatory zonation that the magnetite formed from a hydrothermal fluid.Fig. 14.

Oscillatory zoned high-Si magnetite with elevated concentrations of Al, Ca, and Mg has been reported in magmatic-hydrothermal ore systems such as skarn and IOCG deposits wherein the formation temperature was shown to be at least 400 °C. For example, the silician magnetite reported at the Olympic Dam deposit marks the onset of hydrothermal activity and for which the formation temperature was inferred to be at least 400 °C (Ciobanu et al., 2019; Verdugo-Ihl et al., 2019). At skarn-type deposits, such as Makeng and Chengchao in China, high-Si magnetite grains were shown to form from magmatic-hydrothermal fluids during retrograde stages with formation temperatures of > 450 °C (Hu et al., 2014; Yang et al., 2017; Li et al., 2019). The trace element composition of high-Si magnetite further supports a high temperature hydrothermal formation, although the > 500 °C proposed by Dare et al. (2014; *cf.* Fig. 13A) appear to be too high for the Shepherd Mountain deposit. Based on the similarities between the oscillatory zoned high-Si magnetite at Shepherd Mountain and other magmatic-hydrothermal systems, we argue that the magmatic-hydrothermal fluid at Shepherd Mountain that formed the high-Si magnetite had temperatures of at least 400 °C and was possibly sourced from the same magma that facilitated the formation of the nearby PKM deposit as further discussed in section 5.5. A magmatic-hydrothermal origin for the high-Si magnetite is also supported by the elevated trace element concentrations within high-Si magnetite such as granitophile-group elements (Pb, W, Sn, Mo), HFSE (Ti, Nb, Sc), and REE + Y (Figs. 5, 13A, E). It is noted that Nadoll et al. (2015) suggested that elevated P, REE, and Si contents in magnetite from magmatic-hydrothermal fluids may reflect the presence of apatite and/or silicate micro- to nano-inclusions rather than presence of these elements as solid solution in the magnetite lattice. However, we did not observe any such inclusions during our time-resolved laser ablation ICP-MS analysis. Verdugo-Ihl et al. (2019) attributed relative enrichments of REE + Y and negligible Ni and Cr in silician magnetite at the Olympic Dam to percolation by granite-derived magmatic ore fluids. Elevated concentrations of Al, Mg, Ca, Fe and Si in the Olympic Dam silician magnetite were likely provided from the breakdown of feldspars and mafic minerals during fluid-wall rock interactions (Kontonikas-Charos et al., 2017) and/or a granite-

UNCORRECTED PROOF

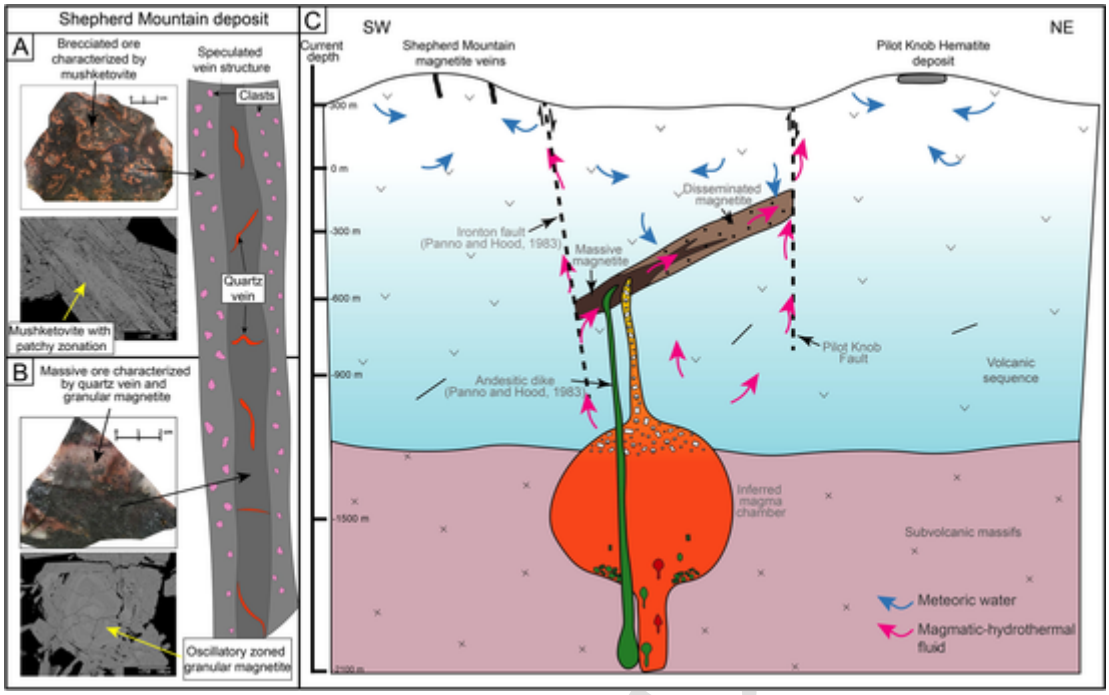


**Fig. 12.** Sketch figure for the formation of deep-seated Pilot-Knob Magnetite deposit (PKM) and shallower Shepherd Mountain deposit illustrating their genetc link. A-B. Illustration of speculated magnetite vein structure wherein the outer parts that are in contact with the wall rock contain brecciated ores that are characterized by muskhetovite with patchy zonation. Central portion of the vein consist of massive ores with quartz veins that are characterized by oscillatory zoned high-Si granular magnetite being replaced by homogeneous low-Si magnetite. C. Illustration of a genetic link displaying the deep-seated PKM deposit and vein-type Shepherd Mountain deposit. The fault on the right was previously mentioned in Panno and Hood (1983); however, for simplicity, it is termed Pilot Knob Fault here.

derived magmatic fluid (Ciobanu et al., 2019). We propose a similar scenario for Shepherd Mountain, wherein a magmatic-hydrothermal fluid with temperature > 400 °C carried Fe and Si from a magma and ascended through the Ironton Fault (Fig. 12; Panno and Hood, 1983) and leached Al, Ca, and Mg from magmatic minerals (e.g., feldspars and biotite/hornblende) during the ascension through the rhyolitic wall rocks (Fig. 12), thus facilitating the formation of high-Si magnetite that is further enriched in REE + Y, Pb, and Sc.

We suggest that the high-Si magnetite forming event is directly related to the mushketovite forming event discussed above. As a second, hotter magmatic-hydrothermal fluid infiltrated and widened the veins, it reduced the specularite to mushketovite due to a drop in the redox state and nucleated high-Si magnetite on the surface of mushketovite, resulting in the formation of the darker domains shown in Fig. 4B. Contemporaneously, the granular high-Si magnetite such as shown in Fig. 4C, F precipitated in the central portions of the veins upon widening. Similar processes, i.e., mushketovitization and subsequent overprinting with high-Si magnetite which are contemporaneous with the formation of high-Si granular magnetite in central parts of the deposit, were also observed at the Mina Justa IOCG deposit in Peru (Hu et al., 2020). The observations from Mina Justa support our speculation that the mushketovitization, followed by the overprinting with high-Si domains in the outer portions of the veins, and the contemporaneous formation of high-Si granular magnetite in the central parts of the veins, reflect the same hydrothermal fluid event with a temperature of > 400 °C.

As opposed to the zoned high-Si magnetite, low-Si magnetite is homogeneous and displays dissolution-reprecipitation textures (Putnis, 2009; Putnis and John, 2010) by replacing the zoned magnetite with sharp and irregular contacts (bright domains in Fig. 4F). The dissolution-reprecipitation textures suggest that a third hydrothermal fluid(s) interacted with the zoned high-Si magnetite, locally dissolved it, and reprecipitated homogeneous secondary magnetite with higher Fe content. Replacement patterns with dissolution-reprecipitation textures generally reflect a mixture of magmatic ore fluids with surface-derived fluids as observed in several magmatic-hydrothermal iron ore systems such as the Makeng skarn Fe deposit in China, the Chadormalu IOA deposit in Iran, and the Mina Justa IOCG deposit in Peru (Heidarian et al., 2016; Yang et al., 2017; Hu et al., 2020b). Several factors may have triggered the dissolution-reprecipitation process, such as changes in temperature, pressure, pH, or oxygen fugacity. As the results of the dissolution-reprecipitation process, the secondary low-Si magnetite contains lesser amount of trace elements such as Si, Ca, Y, Pb, Zr, Hf, W, Sc, Ta, Nb, Sn, Ga, Mg, and Ti except for V (Fig. 13A) compared to the primary high-Si magnetite, which may have been due to a decrease in temperature, as temperature is one of the controlling factors of trace element partitioning into magnetite (Nadoll et al., 2014; Dare et al., 2014). In addition to temperature, the dissolution-reprecipitation process may also have been driven by fluctuations in $fO_2$ which can be assessed via multi-valent element systematics, for example, V and Sn. The oxidation state of V in natural systems varies from 2 + to 5+, with divalent V only being dominant in highly reducing environments ($fo_2$ more reducing than IW buffer; Sutton et al., 2005; Shearer et al., 2006). Vanadium partitioning into magnetite is redox dependent with $V^{3+}$ or $V^{4+}$ being the most compatible species whereas $V^{5+}$ (i.e., under higher oxygen fugacity) is incompatible in magnetite (Toplis and Corgne, 2002; Balan et al., 2006; Righter et al., 2006). Vanadium concentrations in low-Si magnetite (10–110 ppm V) from Shepherd Mountain are slightly higher than in the high-Si magnetite (0.7–66 ppm V; Fig. 6). Therefore, the increase of V in the low-Si magnetite from Shepherd Mountain may imply a decrease in oxygen fugacity when compared to the stage when the high-Si magnetite formed. Lower Sn contents in the low-Si magnetite (0.1–1.1 ppm Sn) compared to the high-Si magnetite (1–6 ppm Sn; Fig. 6A) also support such a decrease in oxygen fugacity at Shepherd Mountain because $Sn^{4+}$ (with 4 + valence state at > FMQ + 3 buffer) substitutes more easily for $Fe^{3+}$ in magnetite under more oxidizing condition (Linnen et al., 1996; Carew, 2004; Barkov et al., 2008). Therefore, the lower Sn contents in low-Si magnetite likely represent a decrease in $fO_2$. Overall, the dissolution-reprecipitation process that formed the low-Si magnetite was likely triggered through late-stage mixing with a third surface-derived, lower

UNCORRECTED

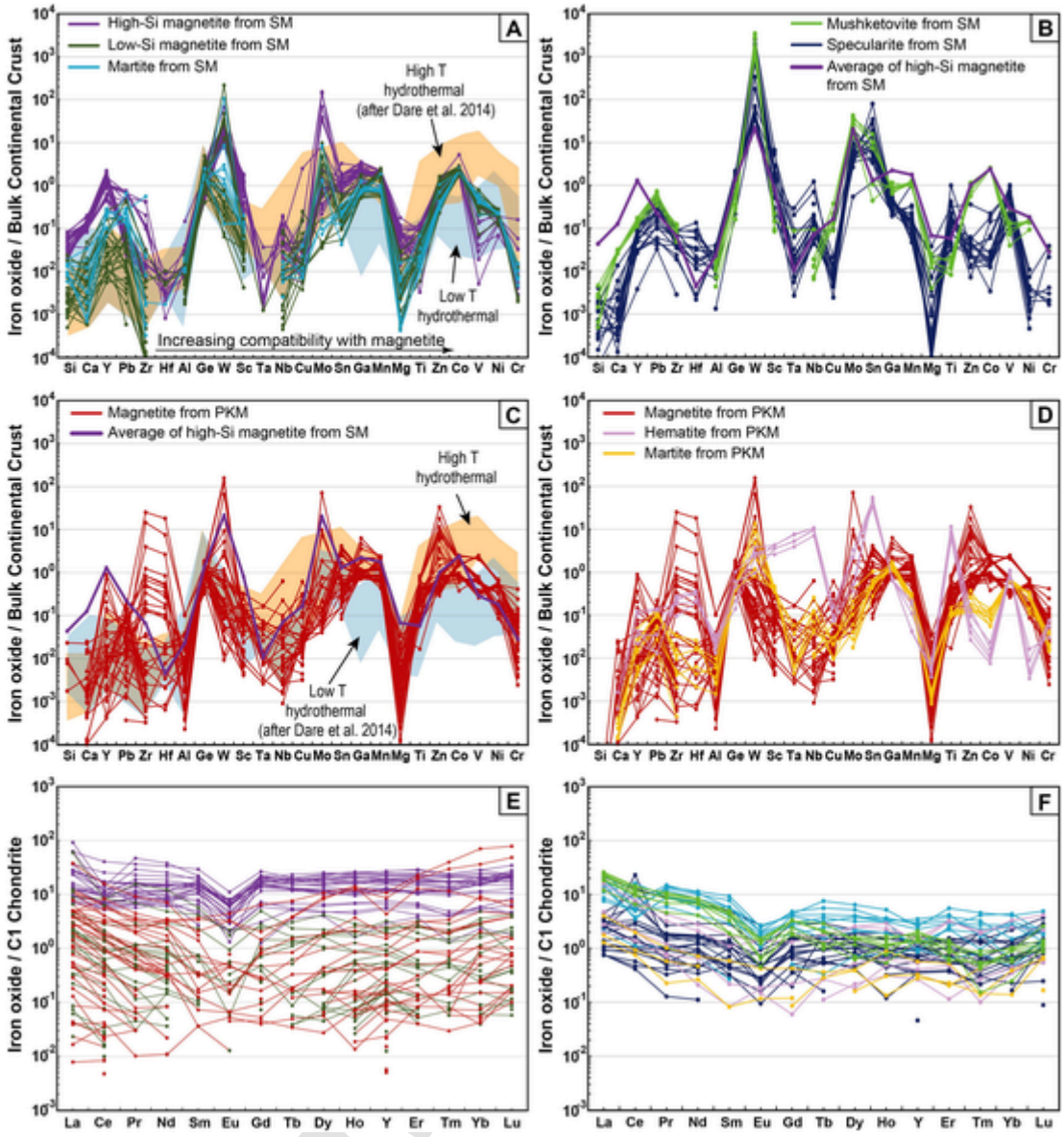


**Fig. 13.** A-D. Bulk continental crust-normalized trace element concentrations of iron oxides from the Shepherd Mountain and Pilot Knob Magnetite deposits analyzed by LA-ICP-MS; E-F. C1 chondrite-normalized REE patterns of iron oxides from the Shepherd Mountain and Pilot Knob Magnetite deposits analyzed by LA-ICP-MS. 24 elements with increasing compatibility to magnetite and high/low temperature hydrothermal fields are taken from Dare et al. (2014). Normalizing values for the bulk continental crust are from Rudnick and Gao (2003); and values for the C1 chondrite are from McDonough and Sun (1995).

temperature meteoric water with an $fO_2$ lower than the high-Si magnetite forming hydrothermal fluid.

In summary, our textural and mineral-chemical observations suggest that at least two generations of magnetite exist that formed after the early precipitation of specularite at the Shepherd Mountain deposit (Fig. 11). The high-Si magnetite formed from a high temperature magmatic-hydrothermal fluid (>400 °C) with a fluctuating composition that facilitated the formation of the oscillatory zonation. Percolation of the fluid through the rhyolitic ash-flow tuffs (Fig. 8A) and minor intermediate volcanic rocks (Panno and Hood, 1983) caused a breakdown of magmatic minerals such as feldspars, biotite and hornblende in the host rocks and provided Al, Ca, and Mg to the ore-forming fluid while Fe and Si may have been extracted from the magma with the exsolving fluid. In contrast, the low-Si magnetite formed through dissolution-reprecipitation processes at temperatures lower than the high-Si magnetite formation temperature upon mixing with a third, likely meteoric, water source.

*5.1.2.1. Formation of late stage martite and specularite at the Shepherd Mountain deposit.* Hematite in the Shepherd Mountain deposit occurs as martitic hematite partially replacing magnetite and mushketovite (Fig. 4A-H), and as late specularite with elongated laths both in breccia and massive ores (Fig. 4C, F, H). It is noted that the specularite discussed in this section is different from the early formed specularite that is fully replaced by mushketovite.

Martite: Martitic alteration of magnetite occurs selectively, often following the colloform texture of magnetite, as shown in Fig. 4D, as well as along $d_{111}$ planes of magnetite as shown in Fig. 4H. The selective martitic alteration was likely caused by a fourth fluid that affected primarily magnetite with low Si, Ca, Al, and Mg concentrations, because high-Si magnetite was demonstrated to be more resistant to martitization based on observations from other locations, such as the Copiapo Nordeste IOCG prospect (González et al., 2018) and the Hamersley BIF (Huberty et al., 2012). The presence of pores and cracks in martite (Figs. 4, 5) suggests that the martitic alteration likely reflects a non-redox transformation, i.e., an interface-coupled

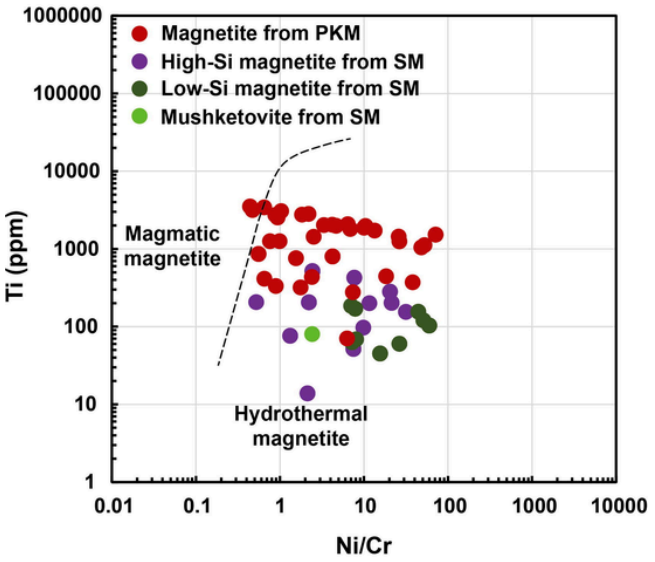


**Fig. 14.** Ni/Cr versus Ti plot to discriminate magmatic magnetite from hydrothermal magnetite, after Dare et al. (2014).

dissolution-reprecipitation reaction (ICDR). During the ICDR process, $Fe^{2+}$ is removed from the crystal structure of magnetite which results in a volume decrease of 33% (Zhao et al., 2019; Xing et al., 2021) and thus creates pore space. Conversely, redox transformation of magnetite to hematite would have resulted in a volume increase by 1.66% (Xing et al., 2021) which is not consistent with the petrographic observations that are indicative of grain shrinkage rather than volume increase (Fig. 4A, D, G). Martitization via non-redox reactions is further supported by the indistinguishable concentrations of V and Sn between magnetite (10 – 110 ppm V, 0.1 – 1.1 ppm Sn) and martite (30 – 86 ppm V, 0.07 – 0.6 ppm Sn), which, due to the redox-sensitive nature of V and Sn discussed above, is indicative of relatively constant redox conditions (Swann and Tighe, 1977; Ohmoto, 2003; Huang et al., 2019). A comparison between the mineral chemistry of martite and the low-Si magnetite it replaces shows that the trace element contents remain relatively constant during the replacement process, with the exception of Pb, W, and REE, which are slightly elevated in martitic hematite (Fig. 13A, B). The retention of pristine trace element abundances during martitization was shown to occur at moderate temperatures of ~ 200 °C (Sidhu et al., 1981; Angerer et al., 2012). The minor additions of Pb, W, and REE indicate that the late-stage fourth fluid was enriched in these elements upon percolation through the rhyolitic/dacitic and intermediate composition volcanic rocks.

Specularite: Textural relationships suggest that specularite at Shepherd Mountain is a late stage phase as its occurrence is restricted to open spaces (Fig. 4C, F, H). However, petrographic observations do not allow us to constrain which formed first, i.e., martitic replacement or specularite formation. Specularite is characterized by greater concentrations of Zr, Hf, Sc, Ta, Nb, Mo, Sn, W, Ti, Mg, and Al when compared to martite (Fig. 13B). Moreover, C1 chondrite normalized REE patterns show lower concentrations of REE in specularite compared to those in martite (Fig. 13F). The differences in composition between martite and specularite suggest that the two hematite groups formed from different fluids, thus implying the presence of a fifth, specularite-forming fluid pulse with a temperature of at least 100 °C and up to 460 °C based on the formation temperature of specularite (e.g., Catling and Moore, 2003; Childress et al., 2020). Elevated HFSE contents in specularite (Fig. 13B) imply that the late-stage specularite-forming ore fluid was F-bearing because F ligands tend to increase HFSE solubility and thus are considered to be critical for transporting HFSE (Montreuil et al., 2016). The presence of a F-bearing fluid is consistent with field observations that identified cross-cutting fluorite veinlets at Shepherd Mountain (*cf.* Nold et al., 2014).

*5.1.2.2. Constraints on fluid(s) from Fe isotope compositions.* Iron isotopic signatures as possible tracers of geological processes have been broadly applied to constrain ore-forming processes for magmatic to magmatic-hydrothermal (Wawryk, 2017; Li et al., 2018; Knipping et al., 2019), hydrothermal (Graham et al., 2004; Markl et al., 2006), and sedimentary deposits (Frost et al., 2007; Mendes et al., 2017; Hu et al., 2020b). The $\delta^{56}$Fe values of mushketovite, which occurs in the brecciated ore (Fig. 2E, F; 4A, B), are −0.55‰ and −0.14‰ (Fig. 7) with an average of −0.35‰. These isotopic signatures likely reflect (i) the formation of the initial specularite from a low temperature (< 400 °C) hydrothermal fluid (Wang et al., 2011; Troll et al., 2019) which is in agreement with the above suggested formation temperature (250 °C – 400 °C), and (ii) the subsequent replacement of specularite by the mushketovite. The petrographic observations discussed above suggest that the mushketovite formed through a dissolution-reprecipitation process in which the primary specularite was reduced to magnetite due to the introduction of a prograde hotter, reducing fluid (Fig. 4A, B). The dissolution and reprecipitation process likely caused a shift toward a lighter Fe isotopic composition because, during dissolution processes, lighter isotopes preferentially partition into fluids which will result in reprecipitation of products from the fluid with lighter Fe isotope compositions (e.g., Weiss, 2013; Troll et al., 2019). The decrease in Fe isotopic values during the dissolution and reprecipitation process is consistent with the reduction process that is required for mushketovite formation as reduction is commonly considered to fractionate Fe towards lighter compositions (Markl et al., 2006).

The $\delta^{56}$Fe values of the magnetite from Shepherd Mountain are −0.26‰ and −0.15‰ (Fig. 7) with an average of −0.21‰. These values are slightly higher compared to that of mushketovite, but lower than the reported $\delta^{56}$Fe values of magnetite from the deeper-seated PKM deposit (0.06‰ – 0.27‰; Childress et al., 2016; Tunnell et al., 2021). The heavier Fe isotopic signatures of Shepherd Mountain magnetite, compared to that of mushketovite, may have resulted from the higher formation temperature (> 400 °C) of the high-Si magnetite as temperature has been shown to be a controlling factor for Fe isotope fractionation in magmatic-hydrothermal systems (Knipping et al., 2019; Troll et al., 2019). Magnetite also shows dissolution and reprecipitation textures in which the partial dissolution of high-Si magnetite resulted in the formation of secondary low-Si magnetite (Fig. 4D, E, F, I). Analogous to the mushketovite, the dissolution and reprecipitation process may have lowered the Fe isotope compositions to negative values. In addition to the dissolution and reprecipitation process, the lighter Fe isotopic composition of magnetite from Shepherd Mountain compared to PKM likely also reflects a temperature dependent fractionation of Fe isotopes during fluid ascent through the Ironton Fault during which heavier isotope were left behind and the cooling ascending fluid was therefore progressively enriched in lighter isotopes (Markl et al., 2006; Wang et al., 2011; Troll et al., 2019).

As opposed to mushketovite and magnetite, the late-stage specularite that formed in open spaces does not show dissolution-reprecipitation textures (Fig. 4F) and has $\delta^{56}$Fe values of −0.19‰ and −0.07‰ with an average of −0.13‰ (Fig. 7). These values are slightly heavier compared to the Fe isotope composition of magnetite and mushketovite at Shepherd Mountain. It is plausible to infer that the ore fluid that formed the late stage specularite had a lighter isotopic signature than the specularite itself as because Markl et al. (2006) showed that hematite that precipitates from an oxidizing fluid has a heavier isotopic signature than the original fluid. The presence of an isotopically light hydrothermal fluid ($\delta^{56}$Fe < -0.19‰ to −0.07‰; i.e., the specularite range) may reflect either a temperature depended fractionation of

UNCORRECTED PROOF

Fe isotopes during fluid and/or fluid mixing with isotopically lighter meteoric water as discussed above for the formation of specularite.

In summary, we argue that the Fe isotope compositions of mushketovite, magnetite, and specularite from the Shepherd Mountain deposit, that formed during different fluid pulses and due to dissolution and reprecipitation processes, reflect a range of processes, including formation temperature, fractionation of Fe isotopes during the ascent of magmatic-hydrothermal fluid through the Ironton Fault, and possibly fluid-mixing with surface-derived meteoric water.

*5.1.2.3. Summary for the formation of the Shepherd Mountain deposit.* Although the Shepherd Mountain ore veins are mined out and stratigraphic relationships are difficult to constrain, we propose that that the breccia ores represent the outer portions of the veins owing to the abundance of wall-rock clasts in the brecciated samples. Conversely, the massive/granular magnetite vein ore does not contain wall rock clasts and consequently is interpreted to represent the central portion of the vein (Fig. 12). The veining and iron oxide mineralization are suggested to have formed through the following processes: specularite was the first mineral to precipitate from an oxidizing magmatic-hydrothermal fluid above the hematite-magnetite buffer at a temperature between 250 and 400 °C when a high-pressure fluid infiltrated the rhyolitic host rock, opening two initially narrow veins and creating a brecciated texture due to high fluid pressure. The Ironton Fault (Panno and Hood, 1983) may have provided a preferred path for fluid ascent. A second pulse of magmatic-hydrothermal ore fluid with a higher temperature (>400 °C) caused a decrease in local oxygen fugacity and the replacement of specularite by mushketovite while preserving the primary specularite texture. The second fluid pulse also widened the veins and caused precipitation of granular, oscillatory-zoned high-Si magnetite wherein the zonation reflects compositional fluctuation of the fluid during percolation. Mixing with surface-derived meteoric waters (third fluid) led to a decrease in temperature and oxygen fugacity which may have promoted the dissolution-reprecipitation process and resulted in the formation of homogeneous low-Si magnetite by replacing high-Si primary magnetite. The low-Si magnetite was subsequently replaced by martite, likely upon draw down of meteoric water (fourth fluid) that caused fluid-mineral reactions at a temperature of ~ 200 °C. A final, fifth pulse of F-bearing fluid facilitated the formation of late specularite in open spaces at temperatures > 100 °C, possibly up to 460 °C. The origin of the fluids and implications for the formation of the Shepherd Mountain deposit within the geodynamic framework of the SE Missouri metallogenic province are discussed in the following section.

### 5.2. Genetic link between the Shepherd Mountain and Pilot Knob magnetite deposits

The Shepherd Mountain and Pilot Knob iron ore systems are nearby (i.e., ~1000 m; Fig. 1C) and were emplaced in the same/similar volcanic rocks as shown in Figs. 8, 9. Therefore, it would be plausible that the Shepherd Mountain and Pilot Knob Magnetite (PKM) deposits are both local expressions of the same magmatic to magmatic-hydrothermal plumbing system. Such a link was previously speculated based on their proximity to one another (Nold et al., 2014), but no geological and/or geochemical studies were conducted to test such a hypothesis. Here we compare whole rock and mineral chemistry data from Shepherd Mountain and PKM (new magnetite LA-ICP-MS data and previously published whole rock data from Tunnell et al. (2021) and Day et al. (2017)) to assess if the two deposits are genetically related.

#### 5.2.1. Insights from iron ore whole-rock chemistry

The Pilot Knob Magnetite deposit has been shown to be magmatic to magmatic-hydrothermal in origin (Fig. 12C), i.e., it is composed of a massive magmatic magnetite ore body in the deeper portion of the deposit that transitions into disseminated magmatic-hydrothermal ore towards shallower levels (Panno and Hood, 1983; Nold et al., 2013; Childress et al., 2016; Tunnell et al., 2021). It is noted that the magmatic origin for the PKM deposit is not fully constrained. For example, an immiscible sodic syenite magma source, as previously suggested by Nold et al. (2013), would be consistent with an emplacement of the PKM deposit in a post-collisional setting (Watts and Mercer, 2020; Tunnell et al., 2021) due to the alkaline nature of magmas that can be expected in such an environment (e.g., Locmelis et al. 2016; Fiorentini et al., 2018; Holwell et al., 2019; Locmelis et al. 2021). However, it is noted that albite in the PKM deposit, which was used to support a syenite magma by Nold et al. (2013), may not necessarily be magmatic/syenitic (Day et al., 2016). Therefore, the magma may have been not syenitic, but perhaps either a silicate melt, as proposed for the Pea Ridge and Bourbon deposits in southeastern Missouri close to Shepherd Mountain (Fig. 1B; Watts and Mercer, 2020), or a more intermediate/andesitic magma as proposed for IOA/IOCG systems in southeast Missouri (Meighan et al., 2019a) and elsewhere (e.g., Simon et al., 2018). The shallower magmatic-hydrothermal magnetite was likely deposited from magmatic ore fluids that were exsolved from the magma that formed the magmatic portion of the deposit (Panno and Hood, 1983; Nold et al., 2013; Childress et al., 2016; Tunnell et al., 2021). The exsolved ore fluids precipitated magnetite by replacing the unwelded sections of an ash-flow tuff and formed a tabular body that is subparallel to the host rock layering within the volcanic sequence (Panno and Hood, 1983).

Iron oxide-mineralized samples from the Pilot Knob Magnetite (13–89 wt% $Fe_2O_3$) and Shepherd Mountain (47–97 wt% $Fe_2O_3$) deposits display similar whole rock patterns in C1 chondrite-normalized and BSE-normalized spidergrams and are notably enriched in LREE (Fig. 10). The bulk compositional similarity of ores between the two deposits may indicate that these two deposits are genetically related. In such a scenario, ore fluid(s) derived from the magma that formed the PKM deposit at depth ascended and utilized the Ironton Fault as a preferred fluid pathway, forming the Shepherd Mountain deposit at a higher stratigraphic level as illustrated in Fig. 12.

*5.2.1.1. Insights from magnetite chemistry.* The compositional similarities in the whole rock ore composition between the Pilot Knob Magnetite and Shepherd Mountain deposit are, at least to some extent, also observed in the magnetite chemistry. It is noted that the low-Si magnetite is a product of dissolution and reprecipitation processes that was not observed at PKM; therefore, the low-Si magnetite is not compared to magnetite from PKM.

Laser ablation ICP-MS analyses of magnetite from PKM and high-Si magnetite from Shepherd Mountain show similar trace element patterns and abundances with respect to Cr, Ni, Mn, Ga, Sn, Nb, Ta, and Ge (Fig. 6A; 13A, C). However, several differences in the trace element composition of magnetite are observed, most notably Ti and V that are depleted in magnetite from Shepherd Mountain, and Si, Ca, Mg and Al that are notably enriched (Fig. 13C). Such compositional variabilities can be expected if the Shepherd Mountain deposit is a surface-near expression of the same plumbing system that formed the PKM deposit at depth due to differences in temperature, redox conditions and draw down of meteoric water which can result in a dilution of elements and cooling of the high T hydrothermal fluids.

It is a notable observation that magnetite from the PKM deposit contains between 70 and 3,500 ppm Ti, of which the higher end values come from deeper (i.e., presumably higher temperature) samples (Fig. 6A). In contrast, the Ti content in high-Si magnetite from the Shepherd Mountain deposit is distinctly lower (15–550 ppm Ti). It is noted that the Ti range reported here for both deposits (15–3,500 ppm Ti) falls within the global range for hydrothermal magnetite (15 – 3,560 ppm; Nadoll et al., 2015). In contrast, magmatic magnetite has been proposed to contain overall higher contents globally between 70 and

UNCORRECTED PROOF

67,100 ppm (Dare et al., 2014; Nadoll et al., 2015; Duparc et al., 2016). Although the Ti contents in magnetite from the PKM and Shepherd Mountain deposits are in the lower range for Ti contents globally, the overlap between the hydrothermal and magmatic ranges does not allow to fully discriminate between magmatic and hydrothermal magnetite solely based on Ti contents. However, when integrated with Ni/Cr contents the magnetite composition indicates a hydrothermal origin (Fig. 11; Dare et al., 2014). The significantly lower Ti contents in magnetite from the Shepherd Mountain deposit may reflect ore formation from ascending, cooling hydrothermal fluids when compared to higher temperature magmatic and magmatic-hydrothermal magnetite from the PKM deposit (Panno and Hood, 1983; Nold et al., 2013; Childress et al., 2016; Tunnell et al. 2021) as Ti contents in magnetite decrease with decreasing temperature (Dare et al., 2014; Nadoll et al., 2014). It is noted that magnetite formation temperature calculations using the empirical Mg geothermometry proposed by Canil and Lacourse (2020) were not feasible due to the significant hydrothermal and chemical weathering of magnetite in the Pilot Knob Magnetite and Shepherd Mountain deposits, which has been shown to result in inaccurate temperature calculations (Palma et al., 2021)

The V contents of high-Si magnetite from Shepherd Mountain (0.7–66.4 ppm V) are overall lower when compared to the PKM deposit (36–343 ppm V; Fig. 6A, 13C). The differences in V contents between the two deposits likely reflect that the fluid that formed Shepherd Mountain was more oxidizing and cooler compared to that at PKM owing to the redox sensitive and temperature dependent nature of V. As mentioned previously, V is more compatible to magnetite under reducing and hotter conditions, which can explain higher V contents as observed in PKM. A similar redox and temperature control on magnetite can also be observed within the PKM deposit (ESM-3) because samples retrieved from 620 to 667 m depth are characterized by 80–343 ppm V while shallower samples from 137 to 177 m depth contain between 36 and 102 ppm V (and 0.7–66.4 ppm V at Shepherd Mountain). Based on these observations, we speculate that magnetite at deeper levels in the PKM deposit formed from a reducing and hotter fluid(s) that became progressively oxidized and cooler upon ascent, resulting in the low V concentrations in the shallower level PKM ore as well as in the surface-near Shepherd Mountain deposit. The progressive decrease in V contents in magnetite with decreasing depth, and, by inference, oxidation and cooling of the ore fluid during ascend, is consistent with a physiochemical connection between the Pilot Knob and Shepherd Mountain deposits within the same plumbing system. In such a context, the elevated Ca, Al, and Mg concentration in the Shepherd Mountain high-Si magnetite likely reflect scavenging of these elements from feldspars, biotite, or hornblende of the wall rock, whereas Fe and Si were extracted from the magma during the exsolution of a magmatic-hydrothermal fluid that ascended through the Ironton Fault. The elevated concentrations of REE + Y within high-Si magnetite from Shepherd Mountain compared to magnetite in PKM (Fig. 13E) may also have resulted from scavenging REE and Y from wall rocks. Alternatively, REE and Y may have originated from the ore fluid exsolved from the magma at depth (i.e., together with Fe and Si) and remained in the ascending magmatic-hydrothermal fluid(s) because the rare earth elements are classified as non-spinel elements and thus would not have partitioned into magnetite at deeper levels (Nadoll et al., 2014).

In summary, our laser ablation ICP-MS data of magnetite from the Shepherd Mountain and PKM deposits indicate that these two deposits have a shared origin based on similar trace element patterns and abundances, most notably Cr, Mn, Ga, Sn, Nb, Ta, and Ge. Differences in Ti, V, Si, Ca, Al, Mg, and REE contents imply that the temperature of the ore forming fluid(s) decreased with decreasing depth while the fluid(s) became more oxidized. An increase in Si, Ca, Al, and Mg contents in magnetite at Shepherd Mountain likely reflects assimilation of these elements from the wall rock during ascent along the Ironton Fault and, integrated with the other discussed trace elements characteristics, may imply that the Pilot Knob Magnetite and Shepherd Mountain deposits are part of the same magmatic-hydrothermal plumbing system.

*5.2.1.2. Insights from hematite chemistry.* The elevated HFSE concentrations in hematite and late specularite in the PKM and Shepherd Mountain deposits, respectively, can also give insight into a possible genetic link between the two deposits (Fig. 6B, C; 13B, D). These hematites are compared because textural relationships suggest that they form during similar late stages within the respective ore formation. Hematite from the PKM deposit is characterized by high Ti concentrations between 25,000–48,000 ppm Ti, which is significantly higher when compared to that in other iron oxides in the PKM deposit (i.e., up to 3,500 ppm; Fig. 6B, C; 13D). It is noted that the Pilot Knob Hematite deposit (PKH), which is located 240 m stratigraphically above the PKM and was shown to be part of the same magmatic-hydrothermal plumbing system as the PKM deposit, is also characterized by high-Ti hematite (<120 ppm up to 26,800 ppm; Tunnell et al., 2021). In comparison, the late-stage specularite from the Shepherd Mountain deposit (Fig. 11) contains between 130 and 4,200 ppm Ti, which is also significantly higher when compared to other iron oxides (i.e., up to 550 ppm Ti) in Shepherd Mountain (ESM-1). Based on the elevated Ti concentrations, an argument can be made that the specularite and hematite from Shepherd Mountain and PKM, respectively, precipitated from the same Ti-rich magmatic-hydrothermal fluid wherein Ti was mobilized as F and Cl complexes as previously suggested for the PKH deposit (Tunnell et al., 2021). The presence of a F-bearing magmatic-hydrothermal fluid is supported by abundant fluorite in the PKM deposit (Nold et al., 2013) as well as fluorite-rich veinlets at Shepherd Mountain (Nold et al., 2014). Analogous to the Ti contents in magnetite, the lower Ti contents in hematite from the Shepherd Mountain and PKH deposits may be indicative of a cooling ore fluid closer to the surface.

In addition to Ti concentrations, both hematite from the PKM deposit and specularite from the Shepherd Mountain deposit are characterized by elevated HFSE (Zr, Hf, Ta, Nb) and W, Sn, and Sc contents when compared to other iron oxide minerals in these deposits (Fig. 13B, D, ESM-1), which may have been sourced from a granitic melt through fluid exsolution as suggested by Meighan et al. (2019b). High field strength elements are commonly considered to be conservative, but several studies have shown that HFSE can be mobilized in a wide range of P-T conditions and their solubility is generally enhanced at high pH conditions and with increasing F contents of the fluids (Vard and Williams-Jones, 1993; Jiang, 2000; Jiang et al., 2005). The mobility of HFSE in F-bearing fluid is in agreement with the observation above that a F-bearing fluid was likely important in the formation of hematite at Pilot Knob and Shepherd Mountain based on the presence of fluorite. The F-bearing fluid also might have collected Ti from a breakdown of mafic minerals and/or hydrothermal rutile that exists in the deeper portions of the PKM deposit (Tunnell et al., 2021). Owing to the elevated Ti, HFSE, W, Sn and Sc contents of hematite from the PKM and Shepherd Mountain deposits, we argue that the same (and/or a similar) F-bearing fluid event formed late stage hematite/specularite both in the PKM and Shepherd Mountain deposits.

*5.2.1.3. Insight from Fe isotope compositions.* As illustrated in Fig. 7, a decrease in $\delta^{56}$Fe signatures is observed in iron oxides from the PKM deposit (heaviest $\delta^{56}$Fe values) to the PKH deposit and Shepherd Mountain deposit (lightest $\delta^{56}$Fe values). The decreasing trend in $\delta^{56}$Fe signatures corresponds to the stratigraphic level of individual deposits as the Shepherd Mountain deposit is located at the stratigraphically highest level whereas PKM is the deepest deposit (e.g., Panno and Hood 1983; Day et al. 2016; Tunnell et al., 2021). We argue that the lighter isotopic signature of magnetite from Shepherd Mountain (i.e., average of $\delta^{56}$Fe = -0.20‰ in average) compared to magnetite from PKM (average of $\delta^{56}$Fe = 0.17‰; Childress et al.

UNCORRECTED PROOF

2016; Tunnell et al. 2021) reflects the temperature dependent fractionation of Fe isotopes during the progressive evolution from magmatic to magmatic-hydrothermal conditions during ascent of the ore fluid through the Ironton Fault. Consequently, the iron isotope signatures of magnetite from Shepherd Mountain and PKM are in agreement with the hypothesis that both deposits were physiochemically connected. We note that no systematic relationship exists between the Fe isotope composition and the trace element composition of the analyzed iron oxide minerals. The absence of a correlation is not surprising, however, as the primary trace element composition of iron oxide minerals is readily modified by hydrothermal processes and chemical weathering (Wen et al., 2017), whereas the Fe isotope composition has been shown to be less susceptible to modification (Childress et al., 2016; Wang et al., 2021).

Because the PKM and PKH deposits were shown to be two endmembers of a magmatic to magmatic-hydrothermal continuum (Tunnell et al., 2021), it can be inferred that the Shepherd Mountain deposit is also genetically related to the PKH deposit. In such a scenario, the near-surface Shepherd Mountain and PKH deposits may be hydrodynamically linked through the PKM deposit at depth as illustrated in Fig. 12. The iron isotopic data support such a model as the late-stage specularite from the Shepherd Mountain deposit has a $\delta^{56}$Fe average value of −0.13‰ which is lighter than $\delta^{56}$Fe values measured for hematite from the PKH deposit (-0.19‰ to 0.30‰ with an average of 0.08‰; Tunnell et al., 2021). The lighter Fe isotopic signature of specularite from Shepherd Mountain likely reflects its emplacement at a higher stratigraphic level which caused more extensive fractionation of Fe isotopes during fluid ascend compared to the PKH deposit. The model for the formation of the Shepherd Mountain and PKM and PKH deposits is further discussed in the next section.

### *5.3. Model for a genetic link between the Shepherd Mountain and Pilot Knob magnetite deposits*

Based on the spatial proximity between the Shepherd Mountain and PKM deposit, field and petrographic observations, geochemical data and stable Fe isotope compositions presented here, we propose that both deposits are local expressions of the same magmatic-hydrothermal plumbing system as illustrated in Fig. 12C. The massive magnetite in the deeper part of the PKM deposit formed from a sodic magnetite syenitic (Nold et al., 2013) or possibly silicate (Watts and Mercer, 2020; Simon et al., 2018) magma and transitioned to disseminated magnetite formed from a magmatic-hydrothermal fluid that exsolved from the magma as previously proposed by Panno and Hood (1983) and Nold et al. (2013). The magmatic-hydrothermal portions of the PKM deposit formed by replacing the unwelded portions of the host ash-flow tuff towards shallower levels (*cf.* Panno and Hood, 1983). The magmatic crystallization and replacement of permeable ash-flow tuff by Fe-rich ore fluid formed a tabular body that is subparallel to the bedding of the volcanic sequence (Panno and Hood, 1983; Nold et al., 2013; Childress et al., 2016; Tunnell et al., 2021). To the northeast of the PKM deposit, the magmatic-hydrothermal fluid ascended further, likely along the Pilot Knob Fault, and formed the PKH deposit by replacing bedded and brecciated volcanic sequence (Tunnell et al., 2021). However, it is noted that the Pilot Knob Fault, which existence was proposed by Panno and Hood (1983), is not exposed. To the southwest of the PKM deposit, several pulses of ore-forming fluid (Fig. 12) ascended along the Ironton Fault, which predates the PKM iron mineralization (Panno and Hood, 1983) and formed the vein-type Shepherd Mountain deposit from hydrothermal fluids as well as meteoric waters as discussed above. In the proposed model, the Fe in all three deposits (Shepherd Mountain, PKM, PKH) is sourced from the same magma, but Fe deposited through different ore-forming processes as a result of different emplacement styles and depths in a common ore-forming system, i.e., vein-hosted (Shepherd Mountain, this study) vs. ash-flow tuff replacement at depth (PKM, Panno and Hood, 1983; Nold et al., 2013) vs. replacement of bedded and brecciated volcano-sedimentary rocks near the surface (PKH; Tunnell et al., 2021).

This scenario is depicted in Fig. 12 in which the deeper magmatic portion of the PKM deposit was derived from a deeper magma chamber (not yet intercepted by drill cores) whereas the shallower portion of the PKM deposit formed from ore fluids exsolved from the magma, with some involvement of surface-derived fluids (Panno and Hood, 1983; Nold et al., 2013; Childress et al., 2016; Tunnell et al., 2021). The Shepherd Mountain and PKH deposits formed from ascending magmatic ore fluids along the faults and represent shallow parts of a single plumbing system. It is noted that dikes of andesitic and aplitic composition are identified in the PKM deposit (Fig. 12), besides the Shepherd Mountain gabbro dike (Panno and Hood, 1983; Nold et al., 2013), that were emplaced at least prior to the last Fe mineralization event; however, its contribution to the ore-forming processes remains to be understood (Panno and Hood, 1983).

## 6. Conclusions

This study investigated the vein-type Shepherd Mountain Fe oxide deposit in the Southeast Missouri Iron Metallogenic Province and its genetic relationship to the Pilot Knob Magnetite and Pilot Knob Hematite deposits. Our findings show that:

- The Shepherd Mountain deposit formed from at least five pulses of magmatic-hydrothermal fluid.
- The mineralization sequence is defined as: (1) Early specularite in the brecciated margins; (2) Mushketovitization of specularite and contemporaneous formation of high-Si magnetite in the center of the veins, both as overgrowths on mushketovite and granular magnetite; (3) Formation of low-Si magnetite following the dissolution of high-Si magnetite and low-Si magnetite reprecipitation; (4) Martitic alteration of magnetite; and (5) Late-stage specularite formation.
- The Pilot Knob Magnetite, Pilot Knob Hematite and Shepherd Mountain deposits are local expressions of the same magmatic-hydrothermal plumbing system connected through local faults.

## Uncited references

Eby (1992).

## Declaration of Competing Interest

The authors declare that they have no known competing financial interests or personal relationships that could have appeared to influence the work reported in this paper.

## Acknowledgements

This paper is part of B. N. T.'s Ph.D. thesis at Missouri S&T. B. N. T. acknowledges funding through a Radcliffe Graduate Scholarship in the Geology & Geophysics program at Missouri S&T. M. L. acknowledges support through the NSF CAREER award 1944552 "Investigating the source, transport and deposition of economically important metals in the lower continental crust".

. Audrey Lavoie at LabMaTer of the UQAC is thanked for carrying out the LA-ICP-MS analysis. We further thank Mr. Andrea Risplendente, University of Milano, for assistance during the microprobe analyses. Lisa Lori from the Doe Run Company and Patrick Scheel from the Missouri Department of Natural Resources are thanked for help during fieldwork. The manuscript benefited greatly from critical reviews by Warren Day and one anonymous reviewer. Nicolas Thebaud and Huayong Chen are thanked for the editorial handling. This is contribution

UNCORRECTED PROOF

#12 of the Missouri S&T MCTF research group and a publication of the O'Keefe Institute for Sustainable Supply of Strategic Minerals at Missouri University of Science and Technology.

## Appendix A. Supplementary data

Supplementary data to this article can be found online at https://doi.org/10.1016/j.oregeorev.2021.104633.

## References


Acosta-Góngora, P., Gleeson, S.A., Samson, I.M., Corriveau, L., Ootes, L., Jackson, S.E., Taylor, B.E., Girard, I., 2018. Origin of sulfur and crustal recycling of copper in polymetallic (Cu-Au-Co-Bi-U ± Ag) iron-oxide-dominated systems of the Great Bear Magmatic Zone, NWT, Canada. Mineral. Deposita 53, 353–376. https://doi.org/10.1007/s00126-017-0736-6.

Aleinikoff, J.N., Selby, D., Slack, J.F., Day, W.C., Pillers, R.M., Cosca, M.A., Seeger, C.M., Fanning, C.M., Samson, I.M., 2016. U-Pb, Re-Os, and Ar/Ar geochronology of rare earth element (REE)-rich breccia pipes and associated host rocks from the Mesoproterozoic Pea Ridge Fe-REE-Au deposit, St. Francois Mountains, Missouri. Econ. Geol. 111, 1883–1914. https://doi.org/10.2113/econgeo.111.8.1883.

Angerer, T., Hagemann, S.G., Danyushevsky, L.V., 2012. Geochemical evolution of the banded iron formation-hosted high-grade iron ore system in the Koolyanobbing greenstone belt, Western Australia. Econ. Geol. 107, 599–644. https://doi.org/10.2113/econgeo.107.4.599.

Ayuso, R.A., Slack, J.F., Day, W.C., McCafferty, A.E., 2016. Geochemistry, Nd-Pb isotopes, and Pb-Pb ages of the Mesoproterozoic Pea Ridge iron oxide-apatite–rare earth element deposit, Southeast Missouri. Econ. Geol. 111, 1935–1962. https://doi.org/10.2113/econgeo.111.8.1935.

Balan, E., De Villiers, J.P.R., Eeckhout, S.G., Glatzel, P., Toplis, M.J., Fritsch, E., 2006. The oxidation state of vanadium in titanomagnetite from layered basic intrusions. Am. Mineral. 91, 953–956. https://doi.org/10.2138/am.2006.2192.

Barkov, A.Y., Martin, R.F., Shi, L., LeBarge, W., Fedortchouk, Y., 2008. Oscillatory zoning in stanniferous hematite and associated W- and Bi-rich minerals from Canadian Creek, Yukon, Canada. Can. Mineral. 46, 59–72. https://doi.org/10.3749/canmin.46.1.59.

Barton, M.D., 2014. Iron oxide (-Cu-Au-REE-P-Ag-U-Co) systems, in: Scott, S.D. (Ed), Geochemistry of mineral deposits. Treatise on Geochemistry, vol 13, 2nd edn. Elsevier, Amsterdam, pp. 515-541. http://dx.doi.org/10.1016/B978-0-08-095975-7.01123-2

Barton, M.D., Johnson, D.A., 1996. Evaporitic-source model for igneous-related Fe oxide–(REE-Cu-Au-U) mineralization. Geology 24, 259–262. https://doi.org/10.1130/0091-7613(1996)024%3C0259:ESMFIR%3E2.3.CO;2.

Beard, B.L., Johnson, C.M., Skulan, J.L., Nealson, K.H., Cox, L., Sun, H., 2003. Application of Fe isotopes to tracing the geochemical and biological cycling of Fe. Chem. Geol. 195, 87–117. https://doi.org/10.1016/S0009-2541(02)00390-X.

Bickford, M.E., Van Schmus, W.R., Karlstrom, K.E., Mueller, P.A., Kamenov, G.D., 2015. Mesoproterozoic-trans-Laurentian magmatism: A synthesis of continent-wide age distributions, new SIMS U-Pb ages, zircon saturation temperatures, and Hf and Nd isotopic compositions. Precambr. Res. 265, 286–312. https://doi.org/10.1016/j.precamres.2014.11.024.

Boni, M., Rankin, A.H., Salvadori, M., 1990. Fluid inclusion evidences for the development of Zn-Pb-Cu-F skarn mineralization in SW Sardinia. Italy. Mineral Mag. 54, 279–287. https://doi.org/10.1180/minmag.1990.054.375.13.

Cabral, A.R., Rosière, C.A., 2013. The chemical composition of specular hematite from Tilkerode, Harz, Germany: Implications for the genesis of hydrothermal hematite and comparison with the Quadrilátero Ferrífero of Minas Gerais. Brazil. Mineral. Deposita 48, 907–924. https://doi.org/10.1007/s00126-013-0459-2.

Canil, D., Lacourse, T., 2020. Geothermometry using minor and trace elements in igneous and hydrothermal magnetite. Chem. Geol. 541, 119576. https://doi.org/10.1016/j.chemgeo.2020.119576.

Catling, D.C., Moore, J.M., 2003. The nature of coarse-grained crystalline hematite and its implications for the early environment of Mars. Icarus 165, 277–300. https://doi.org/10.1016/S0019-1035(03)00173-8.

Carew, M.J., 2004. Controll on Cu-Au mineralization and Fe oxide metasomatism in the Eastern Fold Belt, N.W. Queensland, Australia PhD dissertation. James Cook University, p. 308.

Childress, T.M., Simon, A.C., Day, W.C., Lundstrom, C.C., Bindeman, I.N., 2016. Iron and oxygen isotope signatures of the Pea Ridge and Pilot Knob magnetite-apatite deposits, southeast Missouri, USA. Econ. Geol. 111, 2033–2044. https://doi.org/10.2113/econgeo.111.8.2033.

Childress, T.M., Simon, A.C., Reich, M., Barra, F., Arce, M., Lundsrom, C.C., Bindeman, I.N., 2020. Formation of the Mantoverde iron oxide-copper-gold (IOCG) deposit, Chile: insights from Fe and O stable isotopes and comparisons with iron oxide-apatite (IOA) deposits. Mineral. Deposita 55, 1489–1504. https://doi.org/10.1007/s00126-019-00936-x.

Ciobanu, C.L., Cook, N.J., 2004. Skarn textures and a case study: the Ocna de Fier-Dognecea orefield, Banat, Romania. Ore Geol. Rev. 24, 315–370. https://doi.org/10.1016/j.oregeorev.2003.04.002.

Ciobanu, C.L., Verdugo-Ihl, M.R., Slattery, A., Cook, N.J., Ehrig, K., Courtney-Davies, L., Wade, B.P., 2019. Silician magnetite: Si-Fe-nanoprecipitates and other mineral inclusions in magnetite from the Olympic Dam deposit,South Australia. Minerals 9, 311. https://doi.org/10.3390/min9050311.

Corriveau, L., Montreuil, J.F., Potter, E., 2016. Alteration facies linkages among iron oxide copper-gold, iron oxide-apatite, and affiliated deposits in the Great Bear Magmatic Zone, Northwest Territories, Canada. Econ. Geol. 111, 2045–2072. https://doi.org/10.2113/econgeo.111.8.2045.

Crane, G.W., 1912. The iron ores of Missouri. Missouri Bureau of Geology and Mines. v. 10, 2nd Series, 434 p.

Dare, S.A.S., Barnes, S.-J., Beaudoin, G., 2012. Variation in trace element content of magnetite crystallized from a fractionating sulfide liquid, Sudbury, Canada: Implications for provenance discrimination. Geochim. Cosmochim. Acta 88, 27–50. https://doi.org/10.1016/j.gca.2012.04.032.

Dare, S.A.S., Barnes, S.-J., Beaudoin, G., Méric, J., Boutroy, E., Potvin-Doucet, C., 2014. Trace elements in magnetite as petrogenetic indicators. Mineral. Deposita 49, 785–796. https://doi.org/10.1007/s00126-014-0529-0.

Dare, S.A.S., Barnes, S.J., Beaudoin, G., 2015. Did the massive magnetite "lava flows" of El Laco (Chile) form by magmatic or hydrothermal processes? New constraints fro magnetite composition by LA-ICP-MS. Mineral. Deposita 50, 607–617. https://doi.org/10.1007/s00126-014-0560-1.

Day, W.C., Granitto, M., Ayuso, R., Slack, J., 2017. Geochemical database for iron oxide-copper-cobalt-gold-rare earth element deposits of southeast Missouri (August 2017): U.S. Geological Survey data release, http://dx.doi.org/10.5066/F7P26W67.

Day, W.C., Slack, J.F., Ayuso, R.A., Seeger, C.M., 2016. Regional geologic and petrologic framework for iron oxide ± apatite ± rare earth element and iron oxide copper-gold deposits of the Mesoproterozoic St. Francois Mountains terrane, southeast Missouri, USA. Econ. Geol. 111, 1825–1858. https://doi.org/10.2113/econgeo.111.8.1825.

De Haller, A., Fontboté, L., 2009. The Raúl-Condestable iron oxide copper-gold deposit, central coast of Peru: Ore and related hydrothermal alteration, sulfur isotopes, and thermodynamic constraints. Econ. Geol. 104, 365-384. 10.2113/gsecongeo.104.3.365

Deditius, A.P., Reich, M., Simon, A.C., Suvorova, A., Knipping, J., Roberts, M.P., Rubanov, S., Dodd, A., Saunders, M., 2018. Nanogeochemistry of hydrothermal magnetite. Contrib. Miner. Petrol. 173, 46. https://doi.org/10.1007/s00410-018-1474-1.

Du Bray, E.A., Aleinikoff, J.N., Day, W.C., Neymark, L.A., Burgess, S.D., 2021. Petrology and geochronology of 1.48 to 1.42 Ga igneous rocks in the St. Francois Mountains terrane, southeast Missouri. U.S. Geological survey Professional Paper 1866, 88 p. 10.3133/pp1866.

Dudley, M.A., Nold, J.L., 2001. Mineralogy and ore textures of the Shepherd Mt. iron deposit, Iron Co., Missouri. Trans. Mo. Acad. Sci. 35, 58.

Dudley, M.A., Nold, J.L., 2004. Mineralogy, textures and environments of deposition of iron deposits, St. Francois igneous terrane, southeast Missouri. Abstr. Programs Geol. Soc. Am. 36 (3), 20.

Dünkel, I., 2002. The genesis of East Elba iron ore deposits and their interrelation with Messinian tectonics PhD dissertation. Universitat Tubingen, p. 282.

Duparc, Q., Dare, S.A.S., Cousineau, P., Goutier, J., 2016. Magnetite chemistry as a provenance indicator in Archean metamorphosed sedimentary rocks: Implications for mineral exploration. J. Sed. Res. 86, 1–22. https://doi.org/10.2110/jsr.2016.36.

Dupuis, C., Beaudoin, G., 2011. Discriminant diagrams for iron oxide trace element fingerprinting of mineral deposit types. Mineral. Deposita 46, 319–335. https://doi.org/10.1007/s00126-011-0334-y.

Eby, G.N., 1992. Chemical subdivision of the A-type granitoids: Petrogenetic and tectonic implications. Geology 20, 641–644. https://doi.org/10.1130/0091-7613(1992)020%3C0641:CSOTAT%3E2.3.CO;2.

Fiorentini, M.L., LaFlamme, C., Denyszyn, S., Mole, D., Maas, R., Locmelis, M., Caruso, S., Bui, T.H., 2018. Post-collisional alkaline magmatism as gateway for metal and sulfur enrichment of the continental lower crust. Geochim. Cosmochim. Acta 223, 175–197. https://doi.org/10.1016/j.gca.2017.11.009.

Frost, C.D., von Blanckenburg, F., Schoenberg, R., Frost, B.R., Swapp, S.M., 2007. Preservation of Fe isotope heterogeneities during diagenesis and metamorphism of banded iron formation. Contrib. Miner. Petrol. 153, 211. https://doi.org/10.1007/s00410-006-0141-0.

Giggenbach, W.F., 1984. Mass transfer in hydrothermal alteration systems – a conceptual approach. Geochim. Cosmochim. Acta 48, 2693–2711. https://doi.org/10.1016/0016-7037(84)90317-X.

González, E., Kojima, S., Ichii, Y., Tanaka, T., Fujimoto, Y., Ogata, T., 2018. Silician magnetite from the Copiapó Nordeste prospect of Northern Chile and its implication for ore-forming conditions of iron oxide-copper-gold deposits. Minerals 8, 529. https://doi.org/10.3390/min8110529.

Graham, S., Pearson, N., Jackson, S., Griffin, W., O'Reilly, S.Y., 2004. Tracing Cu and Fe from source to porphyry: in situ determination of Cu and Fe isotope ratios in sulfides from the Grasberg Cu-Au deposit. Chem. Geol. 207, 147–169. https://doi.org/10.1016/j.chemgeo.2004.02.009.

Griffin, W.L., Powell, W.J., Pearson, N.J., O'Reilly, S.Y., 2008. GLITTER: Data reduction software for Lazer Ablation ICP-MS, in: Sylvester, P. (Ed), Laser Ablation-ICP-MS in the Earth Sciences: Current Practices and Outstandingg Issues. Mineral Assoc. Can., Short Course, pp. 308-311.

Groves, D.I., Bierlein, F.P., Meinert, L.D., Hitzman, M.W., 2010. Iron oxide copper-gold (IOCG) deposits through earth history: Implications for origin, lithospheric setting, and distinction from other epigenetic iron oxide deposits. Econ. Geol. 105, 641–654. https://doi.org/10.2113/gsecongeo.105.3.641.

Harlov, D.E., Meighan, C.J., Kerr, I.D., Samson, I.M., 2016. Mineralogy, chemistry, and fluid-aided evolution of the Pea Ridge Fe oxide-(Y + REE) deposit, southeast Missouri. USA. Econ. Geol. 111, 1963–1984. https://doi.org/10.2113/econgeo.111.8.1963.

Heidarian, H., Lentz, D., Alirezaei, S., Peighambari, S., Hall, D., 2016. Using the chemical analysis of magnetite to constrain various stages in the formation and genesis of the Kiruna-type Chadormalu magnetite-apatite deposit, Bafq district, Central Iran. Mineral. Petrol. 110, 927–942. https://doi.org/10.1007/s00710-016-0440-8.

Hildebrand, R.S., 1986. Kiruna-type deposits; their origin and relationship to intermediate subvolcanic plutons in the Great Bear magmatic zone, northwest Canada. Econ. Geol.


UNCORRECTED PROOF

81, 640–659. https://doi.org/10.2113/gsecongeo.81.3.640.
Hitzman, M.W., 2000. Iron oxide-Cu-Au deposits: What, where, when, and why. In: Porter, T. (Ed.), Hydrothermal Iron Oxide Copper-Gold & Related Deposits: A Global Perspective, 1. PGC Publishing, Adelaide, pp. 9–25.
Hofstra, A.H., Meighan, C.J., Song, X., Samson, I., Marsh, E.E., Lowers, H.A., Emsbo, P., Hunt, A.G., 2016. Mineral thermometry and fluid inclusion studies of the Pea Ridge iron oxide-apatite-rare earth element deposit, Mesoproterozoic St. Francois Mountains terrane, southeast Missouri, USA. Econ. Geol. 111, 1985–2016. https://doi.org/10.2113/econgeo.111.8.1985.
Holwell, D.A., Fiorentini, M., McDonald, I., Lu, Y., Giuliani, A., Smith, D.J., Keith, M., Locmelis, M., 2019. A metasomatized lithospheric mantle control on the metallogenic signature of post-subduction magmatism. Nat. Commun. 10, 3511. https://doi.org/10.1038/s41467-019-11065-4.
Hou, T., Charlier, B., Namur, O., 2018. Immiscible hydrous Fe-Ca-P melt and the origin of iron oxide-apatite ore deposits. Nat. Commun. 9, 1–8. https://doi.org/10.1038/s41467-018-03761-4.
Hu, H., Li, J.W., Lentz, D., Ren, Z., Zhao, X.F., Deng, X.D., Hall, D., 2014. Dissolution-reprecipitation process of magnetite from the Chengchao iron deposit: Insights into ore genesis and implication for in-situ chemical analysis of magnetite. Ore Geol. Rev. 57, 393–405. https://doi.org/10.1016/j.oregeorev.2013.07.008.
Hu, J., Wang, H., Tan, J., 2020a. Fe and C isotopes constrain the pathways of hematite and Fe-rich carbonates formation in the Late Neoproterozoic Dahongliutan BIF, NW China. Ore Geol. Rev. 121, 103485. https://doi.org/10.1016/j.oregeorev.2020.103485.
Hu, X., Chen, H., Beaudoin, G., Zhang, Y., 2020b. Textural and compositional evolution of iron oxides at Mina Justa (Peru): Implications for mushketovite and formation of IOCG deposits. Am. Mineral. 105, 397–408. https://doi.org/10.2138/am-2020-7024.
Huang, X.W., Beaudoin, G., 2019. Textures and chemical compositions of magnetite from iron oxide coppe-gold (IOCG) and Kiruna-type iron oxide-apatite (IOA) deposits and their implications for ore genesis and magnetite classification schemes. Econ. Geol. 114, 953–979. https://doi.org/10.5382/econgeo.4651.
Huang, X.W., Boutroy, E., Makvandi, S., Beaudoin, G., Corriveau, L., De Toni, A.F., 2019. Trace element composition of iron oxides from IOCG and IOA deposits: relationship to hydrothermal alteration and deposit subtypes. Mineral. Deposita 54, 525–552. https://doi.org/10.1007/s00126-018-0825-1.
Huberty, J.M., Konishi, H., Heck, P.R., Fournelle, J.H., Valley, J.W., Xu, H., 2012. Silician magnetite from the Dales Gorge member of the Brockman iron formation, Hamersley Group, Western Australia. Am. Mineral. 97, 26–37. https://doi.org/10.2138/am.2012.3864.
Jiang, S.Y., 2000. Controls on the mobility of high field strength elements (HFSE), U, and Th in an ancient submarine hydrothermal system of the Proterozoic Sullivan Pb-Zn-Ag deposit, British Columbia, Canada. Geochem. J. 34, 341–348. https://doi.org/10.2343/geochemj.34.341.
Jiang, S.Y., Wang, R.C., Xu, X.S., Zhao, K.D., 2005. Mobility of high field strength elements (HFSE) in magmatic-, metamorphic-, and submarine-hydrothermal systems. Phys. Chem. Earth. 30, 1020–1029. https://doi.org/10.1016/j.pce.2004.11.004.
Jochum, K.P., Willbold, M., Raczek, I., Stoll, B., Herwig, K., 2007. Chemical characterization of the USGS reference glasses GSA 1g, GSC 1g, GSD 1g, GSE 1g, BCR 2g, BHVO 2g and BIR 1g using EMPA, ID TIMS, ID ICP-MS and LA-ICP-MS. Geostand. Geoanal. Res. 29, 285–302. https://doi.org/10.1111/j.1751-908X.2005.tb00901.x.
Johnson, C.A., Day, W.C., Rye, R.O., 2016. Oxygen, hydrogen, sulfur, and carbon isotopes in the Pea Ridge magnetite-apatite deposit, southeast Missouri, and sulfur isotope comparisons to other iron deposits in the region. Econ. Geol. 111, 2017–2032. https://doi.org/10.2113/econgeo.111.8.2017.
Jonsson, E., Valentin, R.T., Högdahl, K., Harri, C., Weis, F., Nilsson, K.P., Skelton, A., 2013. Magmatic origin of giant 'Kiruna-type' apatite-iron oxide ores in central Sweden. Sci. Rep. 3. https://doi.org/10.1038/srep01644.
Karlstrom, K.E., Ahall, K.I., Harlan, S.S., Williams, M.L., McLelland, J.L., Geisman, J.W., 2001. Long-lived (1.8-0.8 Ga) convergent orogeny in southern Laurentia, its extensions to Australia and Baltica, and implications for refining Rodinia. Precambr. Res. 111, 5–30. https://doi.org/10.1016/S0301-9268(01)00154-1.
Kisvarsanyi, E.B., 1980. Granitic ring complexes and Precambrian hot-spot activity in the St. Francois terrane, Midcontinent region, United States. Geology 8, 43–47. https://doi.org/10.1130/0091-7613(1980)8%3C43:GRCAPH%3E2.0.CO;2.
Kisvarsanyi, E.B., 1981. Geology of the Precambrian St. Francois Terrane, Southeastern Missouri, in: Contribution to Precambrian Geology No. 8. Missouri Department of Natural Resources, Division of Geology and Land Survey, Report of Investigations 64, 58 p.
Kisvarsanyi, G., 1966. Geochemical and petrological study of the Precambrian iron metallogenic province of Southeast Missouri PhD dissertation. University of Missouri-Rolla, Rolla, MO, p. 197 p.
Kisvarsanyi, G., Kisvarsanyi, E.B., 1989. Precambrian geology and ore deposits of the Southeast Missouri Iron Metallogenic Province, in: Max Brown, V., Kisvarsanyi, E.B., Hagni, R.D. (Eds), "Olympic Dam-Type" Deposits and Geology of Middle Proterozoic Rocks in the St. Francois Mountains Terrane, Missouri. Society of Economic Geologists Inc., SEG Guidebook Series 4, pp. 1-40.
Kisvarsanyi, G., Proctor, P.D., 1967. Trace element content of magnetites and hematites, Southeast Missouri Iron Metallogenic Province, USA. Econ. Geol. 62, 449–471. https://doi.org/10.2113/gsecongeo.62.4.449.
Knipping, J.L., Bilenker, L.D., Simon, A.C., Reich, M., Barra, F., Deditius, A.P., Wälle, M., Heinrich, C.A., Holtz, F., Munizaga, R., 2015. Trace elements in magnetite from massive iron oxide-apatite deposits indicate a combined formation by igneous and magmatic-hydrothermal processes. Geochem. Cosmochim. Acta. 171, 15–38. https://doi.org/10.1016/j.gca.2015.08.010.
Knipping, J.L., Fiege, A., Simon, A.C., Oeser, M., Reich, M., Bilenker, L.D., 2019a. In-situ iron isotope analyses reveal igneous and magmatic-hydrothermal growth of magnetite at the Los Colorados Kiruna-type iron oxide-apatite deposit, Chile. Am. Mineral. 104, 471–484. https://doi.org/10.2138/am-2019-6623.
Knipping, J.L., Webster, J.D., Simon, A.C., Holtz, F., 2019b. Accumulation of magnetite by flotation on bubbles during decompression of silicate magma. Sci. Reports 9, 3852. https://doi.org/10.1038/s41598-019-40376-1.
Kontonikas-Charos, A., Ciobanu, C.L., Cook, N.J., Ehrig, K., Krneta, S., Kamenetsky, V.S., 2017. Feldspar evolution in the Roxby Downs Granite, host to Fe-oxide Cu-Au-(U) mineralization at Olympic Dam, South Australia. Ore Geol. Rev. 80, 838–859. https://doi.org/10.1016/j.oregeorev.2016.08.019.
Li, J.X., Qin, K.Z., Li, G.M., Evans, N.J., Huang, F., Zhao, J.X., 2018. Iron isotope fractionation during magmatic-hydrothermal evolution: A case study from the Duolong porphyry Cu-Au deposit, Tibet. Geochem. Cosmochim. Acta. 238, 1–15. https://doi.org/10.1016/j.gca.2018.07.008.
Li, W., Xie, G., M, J., Zhu, Q., Zheng, J., 2019. Mineralogy, fluid inclusion, and stable isotope studies of the Chengchao deposit, Hubei Province, Eastern China: Implications for the formation of high-grade Fe skarn deposits. Econ. Geol. 114, 325-352. 10.5382/econgeo.2019.4633.
Locmelis, M., Fiorentini, M.L., Rushmer, T., Arevalo, R., Adam, J., Denyszyn, S.W., 2016. Sulfur and metal fertilization of the lower continental crust. Lithos 244, 74–93. https://doi.org/10.1016/j.lithos.2015.11.028.
Locmelis, M., Moroni, M., Denyszyn, S.W., Webb, L.E., Fiorentini, M.L., Sessa, G., Caruso, S., Mathur, R., Nanzad, B., 2021. On the formation of magmatic sulphide systems in the lower crust by long-lived mass transfer through the lithosphere: Insights from the Valmaggia pipe, Ivrea Verbano Zone, Italy. Terra Nova 33 (2), 137–149. https://doi.org/10.1111/ter.12499.
Maréchal, C.N., Télouk, P., Albarède, F., 1999. Precise analysis of copper and zinc isotopic compositions by plasma-source mass spectrometry. Chem. Geol. 156, 251–273. https://doi.org/10.1016/S0009-2541(98)00191-0.
Markl, G., von Blanckenburg, F., Wagner, T., 2006. Iron isotope fractionation during hydrothermal ore deposition and alteration. Geochem. Cosmochim. Acta. 70, 3011–3030. https://doi.org/10.1016/j.gca.2006.02.028.
Marschik, R., Fontboté, L., 2001. The Candelaria-Punta del Cobre iron oxide Cu-Au (-Zn-Ag) deposits. Chile. Econ. Geol. 96, 1799–1826. https://doi.org/10.2113/gsecongeo.96.8.1799.
McDonough, W.F., Sun, S.-S., 1995. The composition of the Earth. Chem. Geol. 120, 223–253. https://doi.org/10.1016/0009-2541(94)00140-4.
Meighan, C.J., Hofstra, A.H., Adams, D.T., Marsh, E.E., Lowers, H.A., Koenig A.E., 2019. Absence of magnetite microlites, geochemistry of magnetite veins and replacements in IOA deposits, SE Missouri, USA: relations to intermediate intrusions. Proceedings of the 15th SGA Biennial Meeting, 27-30 August 2019, Glasgow, Scotland, 396-399a.
Meighan, C.J., Hofstra, A.H., Marsh, E.E., Lowers, H.A., Koenig, A.E., 2019. Geochemistry of hematite veins in IOA-IOCG deposits of SE Missouri, USA: relation to felsic magmatism and caldera lakes. Proceedings of the 15th SGA Biennial Meeting, 27-30 August 2019, Glasgow, Scotland, 392-395b.
Menard, J.J., 1995. Relationship between altered pyroxene diorite and the magnetite mineralization in the Chilean iron belt, with emphasis on the El Algarrobo iron deposits (Atacama region, Chile). Mineral. Deposita 30, 268-274. 10.1007/BF00196362.
Mendes, M., Lobato, L.M., Kunzmann, M., Halverson, G.P., Rosière, C.A., 2017. Iron isotope and REE + Y composition of the Cauê banded iron formation and related iron ores of the Quadrilátero Ferrífero. Brazil. Mineral. Deposita 52, 159–180. https://doi.org/10.1007/s00126-016-0649-9.
Menuge, J.F., Brewer, T.S., Seeger, C.M., 2002. Petrogenesis of metaluminous A-type rhyolites from the St. Francois Mountains, Missouri and the Mesoproterozoic evolution of the southern Laurentian margin. Precambr. Res. 113, 269–291. https://doi.org/10.1016/S0301-9268(01)00211-X.
Montreuil, J.F., Potter, E.G., Corriveau, L., Davis, W.J., 2016. Element mobility patterns in magnetite-group IOCG systems: The Fab IOCG system, Northwest Territories, Canada. Ore Geol. Rev. 72, 562–584. https://doi.org/10.1016/j.oregeorev.2015.08.010.
Moreno, J.A., Molina, J.F., Montero, P., Abu Anbar, M., Scarrow, J.H., Cambeses, A., Bea, F., 2014. Unraveling sources of A-type magmas in juvenile continental crust: Constraints from compositionally diverse Ediacaran post-collisional granitoids in the Katerina Ring Complex, southern Sinai, Egypt. Lithos 192–195, 56–85. https://doi.org/10.1016/j.lithos.2014.01.010.
Mucke, A., Cabral, A.R., 2005. Redox and nonredox reactions of magnetite and hematite in rocks. Geochemistry 65, 271–278. https://doi.org/10.1016/j.chemer.2005.01.002.
Nadoll, P., Angerer, T., Mauk, J.L., French, D., Walshe, J., 2014. The chemistry of hydrothermal magnetite: A review. Ore Geol. Rev. 61, 1–32. https://doi.org/10.1016/j.oregeorev.2013.12.013.
Nadoll, P., Mauk, J.L., Leveille, R.A., Koenig, A.E., 2015. Geochemistry of magnetite from porphyry Cu and skarn deposits in the southwestern United States. Mineral. Deposita 50, 493–515. https://doi.org/10.1007/s00126-014-0539-y.
Naslund, H.R., Henríquez, F., Nyström, J.O., Vivallo, W., Dobbs, F.M., 2002. Magmatic iron ores and associated mineralization: Examples from the Chilean High Andes and Coastal Cordillera. In: Porter, T.M. (Ed.), Hydrothermal iron oxide copper-gold and related deposits: A global perspective, v. 2. Adelaide PGC Publishing, pp. 207–226.
Neymark, L.A., Holm-Denoma, C.S., Pietruszka, A.J., Aleinikoff, J.N., Fanning, C.M., Pillers, R.M., Moscati, R.J., 2016. High spatial resolution U-Pb geochronology and Pb isotope geochemistry of magnetite-apatite ore from the Pea Ridge Iron Oxide-Apatite deposit, St. Francois Mountains, southeast Missouri, USA. Econ. Geol. 111, 1915–1933. https://doi.org/10.2113/econgeo.111.8.1915.
Nold, J.L., Davidson, P., Dudley, M.A., 2013. The Pilot Knob Magnetite Deposit in the Proterozoic St. Francois Mountains Terrane, southeast Missouri, USA: A magmatic and hydrothermal replacement iron deposit. Ore Geol. Rev. 53, 446–469. https://doi.org/10.1016/j.oregeorev.2013.02.007.

UNCORRECTED PROOF

Nold, J.L., Dudley, M.A., Davidson, P., 2014. The Southeast Missouri (USA) Proterozoic iron metallogenic province-Types of deposits and genetic relationships to magnetite–apatite and iron oxide–copper–gold deposits. Ore Geol. Rev. 57, 154–171. https://doi.org/10.1016/j.oregeorev.2013.10.002.

Nyström, J.O., Henríquez, F., 1994. Magmatic features of iron ores of the Kiruna-type in Chile and Sweden: Ore textures and magnetite geochemistry. Econ. Geol. 89, 820–839. https://doi.org/10.2113/gsecongeo.89.4.820.

Nyström, J.O., Billström, K., Henríquez, F., Fallick, A.E., Naslund, H.R., 2008. Oxygen isotope composition of magnetite in iron ores of the Kiruna type in Chile and Sweden. J. Geol. Soc. Sweden (GFF) 130, 177–188. https://doi.org/10.1080/11035890809452771.

Ohmoto, H., 2003. Nonredox transformations of magnetite-hematite in hydrothermal systems. Econ. Geol. 98, 157–161. https://doi.org/10.2113/gsecongeo.98.1.157.

Ovalle, J.T., La Cruz, N.L., Reich, M., Barra, F., Simon, A.C., Konecke, B.A., Rodriguez-Mustafa, M.A., Deditius, A.P., Childress, T.M., Morata, D., 2018. Formation of massive iron deposits linked to explosive volcanic eruptions. Sci. Rep. 8, 14855. https://doi.org/10.1038/s41598-018-33206-3.

Palma, G., Reich, M., Barra, F., Ovalle, J.T., del Real, I., Simon, A.C., 2021. Thermal evolution of Andean iron oxide-apatite (IOA) deposits as revealed by magnetite thermometry. Sci. Rep. 11, 18424. https://doi.org/10.1038/s41598-021-97883-3.

Panno, S.V., Hood, W.C., 1983. Volcanic stratigraphy of the Pilot Knob iron deposits, Iron County, Missouri. Econ. Geol. 78, 972–982. https://doi.org/10.2113/gsecongeo.78.5.972.

Pearce, J.A., Harris, N.B.W., Tindle, A.G., 1984. Trace element discrimination diagrams for the tectonic interpretation of granite rocks. J. Petrol. 25, 956–983. https://doi.org/10.1093/petrology/25.4.956.

Pearce, J.A., 1996. A User's Guide to Basalt Discrimination Diagrams, in: Wyman, D.A. (Ed), Trace Elements Geochemistry of Volcanic Rocks: Applications for Massive sulphide Exploration, Geological Association of Canada, Short Course Notes 12, pp. 79-113.

Pollard, P.J., 2006. An intrusion-related origin for Cu-Au mineralization in iron oxide-copper-gold (IOCG) provinces. Mineral. Deposita 41, 179–187. https://doi.org/10.1007/s00126-006-0054-x.

Prendergast, K., Clarke, G.W., Pearson, N.J., Harris, K., 2005. Genesis of pyrite-Au-As-Zn-Bi-Te zones associated with Cu-Au skarns: Evidence from the Big Gossan and Wanagon gold deposits, Ertsberg district, Papua, Indonesia. Econ. Geol. 100, 1021–1050. https://doi.org/10.2113/gsecongeo.100.5.1021.

Putnis, A., 2009. Mineral replacement reactions. Rev. Mineral. Geochem. 70, 87–124. https://doi.org/10.2138/rmg.2009.70.3.

Putnis, A., John, T., 2010. Replacement processes in the Earth's crust. Elements 6, 159–164. https://doi.org/10.2113/gselements.6.3.159.

Reich, M., Deditius, A., Chryssoulis, S., Li, J.W., Ma, C.Q., Parada, M.A., Barra, F., Mittermayr, F., 2013. Pyrite as a record of hydrothermal fluid evolution in a porphyry copper system: A SIMS/EMPA trace element study. Geochem. Cosmochem. Acta. 104, 42–62. https://doi.org/10.1016/j.gca.2012.11.006.

Reich, M., Simon, A.C., Deditius, A., Barra, F., Chryssoulis, S., Lagas, G., Tardani, D., Knipping, J., Bilenker, L., Sánchez-Alfaro, P., 2016. Trace element signature of pyrite from the Los Colorados iron oxide-apatite (IOA) deposit, Chile: a missing link between Andean IOA and iron oxide copper-gold systems? Econ. Geol. 111, 743–761. https://doi.org/10.2113/econgeo.111.3.743.

Rhodes, A., Oreskes, N., 1999. Oxygen isotope composition of magnetite deposits at El Laco, Chile: Evidence of formation from isotopically heavy fluids. Soc. Econ. Geol. Spec. Publ. 7, 333–351. https://doi.org/10.5382/SP.07.11.

Rieger, A.A., Marschik, R., Diaz, M., Holzl, S., Charadia, M., Akker, B., Spangenberg, J.E., 2010. The hypogene iron oxide copper-gold mineralization in the Mantoverde district, northern Chile. Econ. Geol. 105, 1271–1299. https://doi.org/10.2113/econgeo.105.7.1271.

Rieger, A.A., Marschik, R., Díaz, M., 2012. The evolution of the hydrothermal IOCG system in the Mantoverde district, northern Chile: New evidence from microthermometry and stable isotope geochemistry. Mineral. Deposita 47, 359–369. https://doi.org/10.1007/s00126-011-0390-3.

Righter, K., Leeman, W.P., Hervig, R.L., 2006. Partitioning of Ni, Co and V between spinel-structured oxides and silicate melt: importance of spinel composition. Chem. Geol. 227, 1–25. https://doi.org/10.1016/j.chemgeo.2005.05.011.

Rohs, C.R., Van Schmus, W.R., 2007. Isotopic connections between basement rocks exposed in the St. Francois Mountains and the Arbuckle Mountains, southern mid-continent, North America. Int. J. Earth Sci. 96, 599–611. https://doi.org/10.1007/s00531-006-0123-5.

Rudnick, R., Gao, S., 2003. Composition of the continental crust. Treatise Geochem. 3, 1–64. https://doi.org/10.1016/B0-08-043751-6/03016-4.

Seeger, C.M., 2000. Southeast Missouri iron metallogenic province: Characteristics and general chemistry. In: Porter, T.M. (Ed.), Hydrothermal Iron Oxide Copper-Gold & Related Deposits: A Global Perspective, 1. PGC Publishing, Adelaide, pp. 237–248.

Seeger, C.M., 2003. Lithology and alteration assemblages of the Boss iron-copper deposit, Iron and Dent Counties, Southeast Missouri Ph.D. dissertation. University of Missouri-Rolla, Rolla, MO, p. 139.

Shearer, C.K., McKay, G., Papike, J.J., Karner, J.M., 2006. Valence state partitioning of vanadium between olivine-liquid: Estimates of the oxygen fugacity of Y980459 and application to other olivine-phyric Martian basalts. Am. Mineral. 91, 1657–1663. https://doi.org/10.2138/am.2006.2155.

Shiga, Y., 1988. Silician magnetite from the Kamaishi Mine, Japan. Mining Geol. 38, 437–440.

Shimazaki, H., 1998. On the occurrence of silician magnetites. Res. Geol. 48, 23–29. https://doi.org/10.1111/j.1751-3928.1998.tb00004.x.

Shore, M., Fowler, A.D., 1996. Oscillatory zoning in minerals: a common phenomenon. Can. Mineral. 34, 1111–1126.

Sidhu, P.S., Gilkes, R.J., Posner, A.M., 1981. Oxidation and ejection of nickel and zinc from natural and synthetic magnetites. Soil Sci. Soc. Am. J. 45, 641–644. https://doi.org/10.2136/sssaj1981.03615995004500030041x.

Sillitoe, R.H., Burrows, D.R., 2002. New field evidence bearing on the origin of the El Laco magnetite deposit, northern Chile. Econ. Geol. 97, 1101–1109. https://doi.org/10.2113/gsecongeo.97.5.1101.

Sillitoe, R.H., 2003. Iron oxide-copper-gold deposits: An Andean view. Mineral. Deposita 38, 787–812. https://doi.org/10.1007/s00126-003-0379-7.

Simon, A.C., Knipping, J., Reich, M., Barra, F., Deditius, A.P., Bilenker, L., Childress, T., 2018. Kiruna-type iron oxide-apatite (IOA) and iron oxide copper-gold (IOCG) deposits form by a combination of igneous and magmatic-hydrothermal processes: evidence from the Chilean Iron Belt, in: Arribas, A.M., Mauk, J.L. (Eds), Metals, Minerals, and Society. Soc. Econ. Geol. Special Publications No 21, 89-114.

Starkey, M.A., Seeger, C.M., 2016. Mining and exploration history of the Southeast Missouri Iron Metallogenic Province. Econ. Geol. 111, 1815–1823. https://doi.org/10.2113/econgeo.111.8.1815.

Sutton, S.R., Karner, J., Papike, J., Delaney, J.S., Shearer, C., Newville, M., Eng, P., Rivers, M., Dyar, M.D., 2005. Vanadium K edge XANES of synthetic and natural basaltic glasses and application to microscale oxygen barometry. Geochim. Cosmochim. Acta 69, 2333–2348. https://doi.org/10.1016/j.gca.2004.10.013.

Swann, P., Tighe, N., 1977. High voltage microscope of the reduction of hematite to magnetite. Metall. Trans. B 8, 479–487. https://doi.org/10.1007/BF02696936.

Taylor, P.D.P., Maeck, R., De Bièvre, P., 1992. Determination of the absolute isotopic composition and atomic weight of a reference sample of natural iron. Int. J. Mass Spectrom. Ion Proces. 121, 111–125. https://doi.org/10.1016/0168-1176(92)80075-C.

Toplis, M.L., Corgne, A., 2002. An experimental study of element partitioning between magnetite, clinopyroxene and iron-bearing silicate liquids with particular emphasis on vanadium. Contrib. Miner. Petrol. 144, 22–37. https://doi.org/10.1007/s00410-002-0382-5.

Tornos, F., Velasco, F., Hanchar, J.M., 2017. The magmatic to magmatic-hydrothermal evolution of the El Laco deposit (Chile) and its implications for the genesis of magnetite-apatite deposits. Econ. Geol. 112, 1595–1628. https://doi.org/10.5382/econgeo.2017.4523.

Troll, V.R., Weis, F.A., Jonsson, E., Andersson, U.B., Majidi, S.A., Högdahl, K., Harris, C., Millet, M.-A., Chinnasamy, S.S., Kooijman, E., Nilsson, K.P., 2019. Global Fe-O isotope correlation reveals magmatic origin of Kiruna-type apatite-iron-oxide ores. Nat. Commun. 10, 1712. https://doi.org/10.1038/s41467-019-09244-4.

Tunnell, B.N., Locmelis, M., Seeger, C., Mathur, R., Dunkl, I., Sullivan, B., Lori, L., 2021. The Pilot Knob iron ore deposits in southeast Missouri, USA: A high- to low-temperature magmatic-hydrothermal continuum. Ore Geol. Rev. 131, 103973. https://doi.org/10.1016/j.oregeorev.2020.103973.

Van Schmus, W.R., Bickford, M.E., Sims, P.K., Anderson, R.R., Shearer, C.K., Treves, S.B., 1993. Proterozoic geology of the western midcontinent basement, in: Van Schmus, W.R., Bickford, M.E. (Eds), Chapter 4, Transcontinental Proterozoic Provinces, Decade of North American Geology (DNAG). Geological Society of America, pp. 239-259.

Van Schmus, W., Bickford, M., Turek, A., Van der Pluijm, B., Catacosinos, P., 1996. Proterozoic geology of the east-central Midcontinent basement. Geological Society of America Special Papers, pp. 7-32. 10.1130/0-8137-2308-6.7

Vard, E., Williams-Jones, A.E., 1993. A fluid inclusion study of vug minerals in dawsonite-altered phonolite sills, Montreal, Quebec: implications for HFSE mobility. Contrib. Miner. Petrol. 113, 410–423. https://doi.org/10.1007/BF00286931.

Verdugo-Ihl, M.R., Ciobanu, C.L., Cook, N.J., Ehrig, K.J., Courtney-Davies, L., 2019. Defining early stages of IOCG systems: evidence from iron oxides in the outer shell of the Olympic Dam deposit, South Australia. Mineral. Deposita 55, 429–452. https://doi.org/10.1007/s00126-019-00896-2.

Wang, Y., Zhu, X.K., Mao, J.W., Li, Z.H., Cheng, Y.B., 2011. Iron isotope fractionation during skarn-type metallogeny: A case study of Xinqiao Cu-S-Fe-Au deposit in the Middle-Lower Yangtze valley. Ore Geol. Rev. 43, 194–202. https://doi.org/10.1016/j.oregeorev.2010.12.004.

Wang, Y., Xiangkun, Z., Tang, C., Mao, J., Chang, Z., 2021. Discriminate between magmatic- and magmatic-hydrothermal ore deposits using Fe isotopes. Ore Geol. Rev. 130, 103946. https://doi.org/10.1016/j.oregeorev.2020.103946.

Watts, K.E., Mercer, C.N., 2020. Zircon-hosted melt inclusion record of silicic magmatism in the Mesoproterozoic St. Francois Mountains terrane, Missouri: Origin of the Pea Ridge iron oxide-apatite-rare earth element deposit and implications for regional crustal pathways of mineralization. Geochem. Cosmochim. Acta. 272, 54–77. https://doi.org/10.1016/j.gca.2019.12.032.

Wawryk, C.M., 2017. An investigation into iron isotope systematics in felsic magmas and their associated magmatic-hydrothermal ore deposits Ph.D. dissertation. The University of Adelaide, Australia, p. 280.

Weis, F., 2013. Oxygen and iron isotope systematics of the Grängesberg mining district (GMD), Central Sweden Ph.D. dissertation. Uppsala University, Sweden, p. 83.

Wen, G., Li, J.W., Hofstra, A.H., Koenig, A.E., Lowers, H.A., Adams, D., 2017. Hydrothermal reequilibration of igneous magnetite in altered granitic plutons and its implications for magnetite classification schemes: Insights from the Handan-Xingtai iron district, North China Craton. Geochem. Cosmochim. Acta 213, 255–270. https://doi.org/10.1016/j.gca.2017.06.043.

Westhues, A., Hanchar, J.M., Voisey, C.R., Whitehouse, M.J., Rossman, G.R., Wirth, R., 2017. Tracing the fluid evolution of the Kiruna iron oxide apatite deposits using zircon, monazite, and whole rock trace elements and isotopic studies. Chem. Geol. l 466, 303–322. https://doi.org/10.1016/j.chemgeo.2017.06.020.

Whalen, J.B., Currie, K.L., Chappell, B.W., 1987. A-type granites: geochemical characteristics, discrimination and petrogenesis. Contrib. Miner. Petrol. 95, 407–419. https://doi.org/10.1007/BF00402202.

UNCORRECTED PROOF

Whitmeyer, S.J., Karlstrom, K.E., 2007. Tectonic model for the Proterozoic growth of North America. Geosph. 3, 220–259. https://doi.org/10.1130/GES00055.1.
Williams, P.J., Barton, M.D., Johnson, D.A., Fontboté, L., De Haller, A., Mark, G., Oliver, N.H., Marschik, R., 2005. Iron oxide copper-gold deposits: Geology, space-time distribution, and possible modes of origin. Econ. Geol. 100th Anniversary 371–405. https://doi.org/10.5382/AV100.13.
Xing, Y., Brugger, J., Etschmann, B., Tomkins, A.G., Frierdich, A., Fang, X., 2021. Trace element catalyses mineral replacement reactions and facilitates ore formation. Nat. Commun. 12, 1388. https://doi.org/10.1038/s41467-021-21684-5.
Yang, Y.L., Ni, P., Pan, J.Y., Wang, G.G., Xu, Y.F., 2017. Constraints on the mineralization processes of the Makeng iron deposit, eastern China: Fluid inclusion, H-O isotope and magnetite trace element analysis. Ore Geol. Rev. 88, 791–808. https://doi.org/10.1016/j.oregeorev.2016.11.018.
Yesavage, T., Stinchcomb, G.E., Fantle, M.S., Sak, P.B., Kasznel, A., Brantley, S.L., 2016. Investigation of a diabase-derived regolith profile from Pennsylvania: Mineralogy, chemistry and Fe isotope fractionation. Geoderma 273, 83–97. https://doi.org/10.1016/j.geoderma.2016.03.004.
Zhao, J., Brugger, J., Pring, A., 2019. Mechanism and kinetics of hydrothermal replacement of magnetite by hematite. Geosci. Front. 10, 29–41. https://doi.org/10.1016/j.gsf.2018.05.015.

UNCORRECTED PROOF